

Institut für Angewandte Physik  
der Universität Bonn

Wegelerstraße 8  
53115 Bonn

---

# Simultaneous Non-Destructive State Detection of Neutral Atoms

---

von  
Yannik Völzke

Masterarbeit in Physik

angefertigt im  
Institut für Angewandte Physik

vorgelegt der  
Mathematisch-Naturwissenschaftlichen Fakultät  
der Rheinischen Friedrich-Wilhelms-Universität Bonn

November 2014

Referent: Prof. Dr. Dieter Meschede  
Koreferent: Prof. Dr. Stefan Linden



# Summary

The present work investigates a non-destructive hyperfine state detection method for neutral atoms in an one dimensional optical lattice. The atoms are exposed to near resonant light and from their fluorescence image their internal state can be extracted. Additionally a compression method is presented to densify an atomic ensemble in this trap.

Chapter 1 presents the experimental setup for trapping a small atomic ensemble in an one dimensional lattice. Chapter 2 focuses on the compression sequence and its efficiency. Chapter 3 is devoted to the state detection of well separated individual atoms. It provides detailed studies of the imaging system and the state dependent imaging is investigated experimentally and theoretically.

In chapter 4 a Bayesian analysis of the fluorescence images is used to improve the state detection fidelity. In chapter 5 the state detection is performed for groups of atoms that cannot be individually resolved. For two atoms this is done experimentally and the many atom case is simulated to compare different analysis methods.

Finally, chapter 6 summarizes the results of this thesis and gives a short outlook.



# Contents

<b>1</b>	<b>Introduction</b>	<b>1</b>
<b>2</b>	<b>Experimental Setup</b>	<b>3</b>
2.1	Optical Transition in Rubidium . . . . .	3
2.2	Magneto-Optical Trap . . . . .	4
2.2.1	Working Principle . . . . .	5
2.2.2	Experimental Realisation . . . . .	5
2.3	Dipole Trap . . . . .	6
2.3.1	Dipole Force . . . . .	6
2.3.2	Standing Wave and Running Wave Configuration . . . . .	8
2.3.3	Experimental Realisation . . . . .	8
2.4	Imaging of Neutral Atoms . . . . .	9
2.4.1	Detection System . . . . .	9
2.4.2	State independent Imaging . . . . .	9
<b>3</b>	<b>Creation of a Dense Ensemble of Neutral Atoms</b>	<b>11</b>
3.1	The Basic Principle . . . . .	11
3.2	The Harmonic Approximation . . . . .	12
3.2.1	Compression in the Harmonic Approximation . . . . .	13
3.3	The Experimental Realization . . . . .	14
3.4	The Simulation . . . . .	16
3.5	Crossed Beam Compression . . . . .	20
<b>4</b>	<b>Non-Destructive Free Space Hyperfine State Detection</b>	<b>23</b>
4.1	State Dependent Imaging . . . . .	24
4.2	The Detection Error . . . . .	25
4.3	Experimental Sequence and Analysis Program . . . . .	26
4.4	The Camera . . . . .	29
4.4.1	Working Principle . . . . .	29
4.4.2	Important Functions . . . . .	29
4.4.3	Camera Noise . . . . .	31

4.5	Modelling the Count Distribution . . . . .	36
4.6	Monte-Carlo Simulation . . . . .	39
4.6.1	Working Principle of the Simulation . . . . .	39
4.6.2	Results of the Simulation . . . . .	40
4.7	Experimental results . . . . .	41
4.7.1	The first try . . . . .	42
4.7.2	Frequency Scan . . . . .	42
4.7.3	Comparison of the Model and Experimental Data . . . . .	43
4.7.4	Parameter Scan with Analytic Model . . . . .	45
4.7.5	Optimized Magnetic Fields . . . . .	45
<b>5</b>	<b>Use Spatial Information to Improve State Detection Fidelity</b>	<b>49</b>
5.1	Bayesian Analysis . . . . .	49
5.1.1	Bayes' Theorem . . . . .	49
5.1.2	Weighting . . . . .	51
5.1.3	Single Pixel Count Distributions . . . . .	51
5.2	Experimental Results . . . . .	53
5.3	Monte Carlo Simulation . . . . .	54
5.3.1	Principle of the Simulation . . . . .	54
5.3.2	Results of the Simulation . . . . .	55
<b>6</b>	<b>State Detection with Multiple Atoms</b>	<b>57</b>
6.1	Two Atom Case . . . . .	57
6.1.1	Bayesian Analysis . . . . .	58
6.1.2	Experimental realisation . . . . .	59
6.2	Simulated Many Atom State Detection . . . . .	59
6.2.1	Different Analysis Methods . . . . .	59
6.2.2	The Simulation . . . . .	62
6.2.3	Simulation Results . . . . .	63
<b>7</b>	<b>Conclusion and Outlook</b>	<b>65</b>
<b>A</b>	<b>Appendix</b>	<b>67</b>
A.1	Formulae and Calculations . . . . .	67
A.1.1	Formulae . . . . .	67
A.1.2	Calculations . . . . .	68
A.2	Proofs . . . . .	69
A.2.1	Proof that Bayes' theorem lead to likelihood functions . . . . .	69
A.2.2	Proof that the update rule holds . . . . .	70

# Chapter 1

## Introduction

Information transfer is one of the key elements of 21st centuries technology. Making use of the laws of quantum mechanics, Quantum Information science has the potential to make fundamentally change the way information is transferred. Quantum Communication could lead to absolutely secure transmission [1]. Furthermore, by transferring quantum states between multiple parties entire quantum networks could be build [2].

The generation of entanglement over very long distances is one of the main challenges for the realization of this ideas. A very prominent way of generating remote entanglement is the so called Duan Lukin Cirac Zoller (DLCZ) protocol [3]. This protocol uses quantum memories as quantum repeaters to swap and thereby extend the entanglement [3]. In order to work efficiently a very high coupling strength between flying and stationary qubits is desirable [4].

Two methods are established for achieving this: Cooperative interaction and cavity enhancement. When an ensemble of indistinguishable atoms absorbs a photon a Dicke state is formed. The effective atom light coupling scales in this case proportional with the square root of the atom number [5]. Alternatively, stationary qubits can be placed inside a resonant cavity where the Purcell effect strongly enhances the atom-light interaction [6].

First demonstrations of quantum memories have been for example realized in solid state systems [7, 8], an atomic ensemble in a ring cavity [9] and in free space [10], and with a single photon inside an ultra high finesse cavity [11].

In our research group, we want to used a small atomic ensemble of atoms inside a fibre based cavity which combines the beneficial effects of Purcell enhancement and collective enhancement. Such fibre based cavities have for example very successfully be implemented in on chip quantum circuits [12]. Due to their small mode volume fibre based cavities require a smaller finesse to achieve the same coupling regime [13]. This makes them more stable and

allows a higher photonic bandwidth [13].

To benefit maximally from the collective enhancement we are interested in generating an atomic ensemble which is as dense as possible. The first part of this thesis is about creating such dense ensembles of neutral atoms. These studies are performed on neutral atoms inside an optical dipole trap.

Optically trapped neutral atoms are widely used in experiments in quantum metrology [14], quantum simulation [15] and quantum information processing [16]. In all those experiments atomic qubits are manipulated and information is extracted from their internal states. This state detection is usually done destructively by removing all atoms in a given state [17]. A non-destructive method for the state detection would strongly increase the measurement rate in these systems.

Previously non-destructive state detection in free space has been realized for single atoms only [18, 19]. Here, we demonstrate for the first time the non-destructive simultaneous state detection of multiple atoms. but not for the simultaneous detection of multiple atoms.

# Chapter 2

## Experimental Setup

All our experiments are done with Rubidium 87 atoms inside a ultra high vacuum (UHV) apparatus. The atoms are trapped in a standing wave dipole trap and imaged with an emCCD camera. In this chapter I will explain the experimental setup in more detail.

### 2.1 Optical Transition in Rubidium

The electronic ground state of Rubidium 87 is the  $5^2S_{1/2}$  [20] state with nuclear spin is  $3/2$  [20]. In all experiments we use the  $D_2$  line which is the transition between the ground and the  $5^2P_{3/2}$  state at about 780 nm.

Figure 2.1 shows the hyperfine splitting of the  $D_2$  line. The hyperfine splittings of the ground states is much greater than the hyperfine splitting of the excited states. The higher the hyperfine quantum number the greater is the hyperfine splitting between two neighbouring excited states. As a short hand notation I will use  $F'$  to refer to the hyperfine state of the excited state and  $F$  to the hyperfine state of the ground state. In the same manner I will use  $m_F$  and  $m'_F$ .

Not shown in figure 2.1 is the Zeeman splitting of the transition. All hyperfine states contain Zeeman sublevels with integer quantum numbers between  $m_F = \pm F$ .

The interaction between the light fields and the atoms is dominated by dipole interaction. All transitions therefore have to fulfil the selection rules

$$\Delta F \in \{-1, 0, 1\} \tag{2.1a}$$

$$\Delta m_F \in \{-1, 0, 1\}, \quad m_F = 0 \rightarrow m'_F = 0 \text{ forbidden.} \tag{2.1b}$$

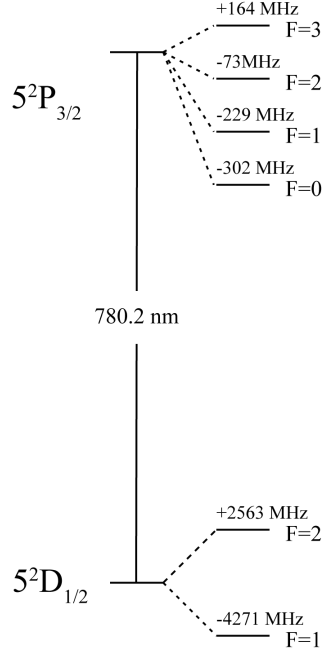


Figure 2.1: Hyperfine structure of Rubidium 87  $D_2$  transitions. The excited state is the  $5^2P_{3/2}$  which is split into four hyperfine states. Levels not to scale.

Here,  $\Delta F$  is the change in hyperfine and  $\Delta m_F$  the change of Zeeman quantum number. The scattering rate  $R_{\text{sc}}$  of an atom that is exposed to monochromatic light is given by [20]

$$R_{\text{sc}} = \frac{\Gamma}{2} \frac{s}{1 + 4(\Delta/\Gamma)^2 + s}, \quad (2.2)$$

where  $\Gamma$  is the natural linewidth,  $s$  the intensity normalized by the saturation intensity and  $\Delta$  the detuning.

## 2.2 Magneto-Optical Trap

A magneto-optical trap (MOT) forms the first stage in cooling and trapping the atoms. A MOT was first realised in 1987 [21] and was awarded in 1997 with the Nobel price in physics. Today hardly any experiment with single trapped atoms would be possible without a MOT.

### 2.2.1 Working Principle

The MOT is based on the principle of velocity and spatially dependent light scattering forces.

#### Optical molasses

An optical molasses typically consists of six laser beams although setups with only four beams are possible [22].

The laser light is red detuned to a cyclic transition. If an atom moves towards the beam it Doppler shifts the beam to the blue and it is more likely that it absorbs a photon of this beam than from the others. In the absorption process the momentum of the photon is transferred to the atom. When the atom spontaneously emits a photon it gains momentum in a random direction. After many repetitions of this process the overall momentum transferred by the emission of photons averages to zero. Hence the temperature of an atomic ensemble within the molasses is lowered [23].

#### Position Dependent Potential

The molasses cools the atoms but this is not sufficient to trap them. Two coils in Anti-Helmholtz configuration give a position dependent magnetic field which shifts the Zeeman sublevels. The zero of the magnetic field lies at the intersection of the molasses beams. In the centre of the trap those coils provide a linearly increasing magnetic field in all three dimensions.

Figure 2.2 shows how the space dependent potential is formed. In a MOT one of the counter propagating molasses beams is  $\sigma^+$  and the other one is  $\sigma^-$  polarized.

For positive magnetic fields the Zeeman shift brings the  $\sigma^-$  transition closer to resonance which results in a higher scattering rate. This results in a force in parallel to the propagation direction of the  $\sigma^-$  beam. On the other side the effect is the other way around. The beams are propagating such that the resulting force always points towards the center and therefore a trap is formed.

### 2.2.2 Experimental Realisation

We use three laser beams that intercept each other perpendicularly. The beams are back reflected into themselves. With a  $\lambda/4$  plate that is passed two times we rotate the polarization from  $\sigma^-$  in the original beam to  $\sigma^+$  polarization in the retro reflected beam. The beams are red detuned (10 MHz) from the  $F = 2 \rightarrow F' = 3$  transition and have a power of 20  $\mu\text{W}$  and a waist

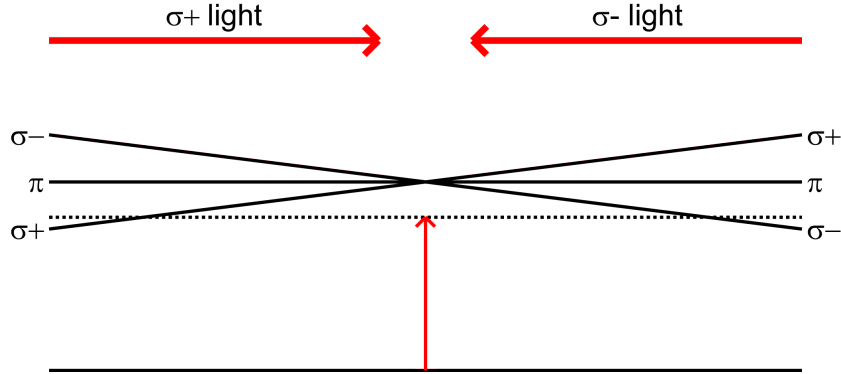


Figure 2.2: The magnetic field shifts the Zeeman sublevels. On the left side of the zero the shifting causes the  $\sigma^+$  transition to be closer to the resonance than the  $\sigma^-$  ones. Therefore the atoms more likely absorb a photon of the  $\sigma^+$  beam. This causes a radiation force towards the center. On the right side the Zeeman shift is in the other direction which gain leads to a radiation force towards the center.

of  $350 \mu\text{m}$ .

Off resonantly excited atoms can decay into the  $F = 1$  state and do not interact with the cooling light any more. A laser resonant to the  $F = 1 \rightarrow F' = 2$  transition acts as a repumper and ensures that the atoms stay on this cyclic transition. The repumper excites the atom in the  $F' = 2$  state until they decay in the  $F = 2$  state and interact with the cooling light again.

With this MOT we trap typically 5 to 10 atoms in about 3 s. The background gas pressure is about  $10^{-10}$  mbar.

## 2.3 Dipole Trap

In the MOT the atoms are confined in a volume of several tens of micrometers. We overlap the MOT with a strongly focused dipole trap in which we can trap and localize individual atoms.

### 2.3.1 Dipole Force

In a classical picture a laser field contains an oscillating electric and magnetic field. The oscillating electric field induces a dipole moment in the atoms. This can be explained in the Lorentz model picture of an atom.

In the Lorentz model the atom consists of an electron (mass  $m_e$ , charge

$-e$ ) that is elastically bound by the harmonic potential of the core ( $M \gg m_e$ ). An external light field with frequency  $\omega$  which has the form  $\vec{E}(t) = \vec{E}_0 \exp(i\omega t) + c.c.$  drives oscillations of the electron. This leads to an induced dipole moment  $\vec{d} = \alpha \vec{E}(t)$  with the complex polarization  $\alpha$ . Dipole radiation leads to damping rate  $\Gamma_\omega = \frac{e^2 \omega^2}{6\pi\epsilon_0 m_e c^3}$ . The electronic equation of motion is given by [24, 25]

$$\ddot{\vec{x}} + \Gamma_\omega \dot{\vec{x}} + \omega_0^2 \vec{x} = -e\vec{E}(t), \quad (2.3)$$

where  $\omega_0$  is the oscillation frequency of the electron. Using  $\vec{d}(t) = -e\vec{x}(t) = \alpha \vec{E}(t)$  and the stationary solution of formula 2.3 one can compute the polarization as [24, 25]

$$\alpha = \frac{e^2}{m_e} \frac{1}{\omega_0^2 - \omega^2 + i\Gamma_\omega \omega}. \quad (2.4)$$

The dipole potential  $U = \frac{1}{2} \vec{d} \vec{E}$  is time dependent. Therefore, the effective potential is given by the time average of the potential

$$U(x) = -\vec{E}_0^2 \text{Re}(\alpha) = -\frac{I(\vec{x})}{2\epsilon c} \text{Re}(\alpha). \quad (2.5)$$

The potential is proportional to the intensity of the light field. The gradient of the potential gives the dipole force which pushes the atoms towards the minima of the potential. The minima of the potential is given by the minima of the intensity if  $\omega_0 < \omega$  (blue detuning) and by the maxima of the intensity if  $\omega_0 > \omega$  (red detuning) [24, 25].

Using the rotating wave approximation one finds that the potential is inversely proportional to the detuning while the scattering rate due to the dipole trap is inversely proportional to the detuning squared [24].

A quantum mechanical treatment of a two level atom leads to the same expression for the ground state [24]. For the excited state the potential changes sign. This means that an attractive potential turns repulsive whenever an atom gets excited [24].

In a multi level atom all transition play a role and the situation is more complicated [24].

### 2.3.2 Standing Wave and Running Wave Configuration

All state detection experiments will be done in the so called standing wave configuration. During the compression experiment we switch between a standing wave and a running wave potential.

The running wave configuration is caused by the potential of a single Gaussian beam. The resulting trapping potential  $U(\vec{x})$  is proportional to the intensity.

$$U(z, r) = U_0 \underbrace{\frac{w_0}{w(z)} \exp\left(-\frac{2r^2}{w(z)^2}\right)}_{U_{\text{rw}}(z,r)}, \quad U_0 = \frac{\text{Re}(\alpha)I(0)}{2\epsilon_0 c} \quad (2.6)$$

Here  $w_0$  is the beam waist,  $z$  is the coordinate in propagation direction,  $r$  is the distance from the optical axis and  $w(z) = w_0 \sqrt{1 + \left(\frac{z\lambda}{\pi w_0^2}\right)^2}$  is the beam waist at position  $z$ .

A standing wave configuration is built up by two counter propagating beams of the same intensity. The beams interfere with each other and give an alternating pattern of maximal and minimal intensities. The trapping potential in this case is given by

$$U(z, r) = 4U_0 \underbrace{\frac{w_0}{w(z)} \exp\left(-\frac{2r^2}{w(z)^2}\right) \cos\left[kz - \arctan\left(\frac{z}{zR}\right) - \frac{kr^2}{2R(z)}\right]}_{U_{\text{sw}}(z,r)}, \quad (2.7)$$

where  $k = 2\pi/\lambda$  is the wave number. For perfectly overlapping beams the trap depth is 4 times the trap depth of a standing wave dipole trap with the same intensity and wavelength.

Figure 2.3 shows an intensity plot of the standing wave potential.

### 2.3.3 Experimental Realisation

For the dipole trap we use a laser with 860 nm wavelength. The light that is red detuned from the Rubidium D<sub>2</sub> line by 80 nm is emitted by a Titanium Sapphire laser. The light is split into two arms and is passed through one tapered amplifier in each arm to increase the power. The two arms are aligned to counterpropagate and are focussed down to the same spot with a waist of 5  $\mu\text{m}$  by two high numerical aperture lenses.

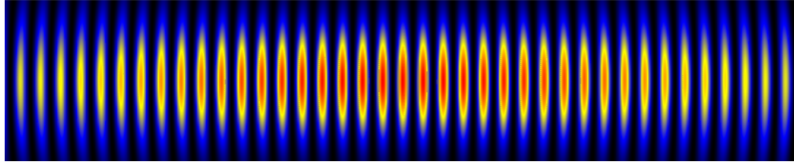


Figure 2.3: Intensity of a running wave potential for  $w_0 = 2\lambda$ . Red means the highest intensity and black the lowest.

By means of a Acousto Optic Modulators (AOM) the intensity in each arm can be changed. To form a standing wave potential both arms have the same intensity.

## 2.4 Imaging of Neutral Atoms

In order to observe the cooled and trapped atoms we perform fluorescence imaging.

### 2.4.1 Detection System

When we image the atoms we illuminate them using the molasses beams. The fluorescence light has a wavelength of 780 nm and is collected by a high numerical aperture lens. The light which is emitted in the antipodal direction is retro reflected to further increase the collection efficiency.

The fluorescence light is sent on an electron multiplying charge coupled device (emCCD) camera. We use an Andor Ixon 3 camera model DU-897D-CS0-#BV with  $512 \times 512$  pixels á  $16\mu\text{m} \times 16\mu\text{m}$  and a quantum efficiency of around 70 % for light with a wavelength of 780 nm [26]. To obtain an image we expose the camera for time spans from 5 ms to 100 ms. Figure 2.4 depicts the imaging system.

### 2.4.2 State independent Imaging

Normal or state independent imaging enables us to detect individual atoms and get their position in the dipole trap.

The atoms are trapped in the dipole trap and illuminated by the cooling and repumping beams. In this way all atoms independent of their initial hyperfine state scatter photons during the whole imaging time. Their fluorescence signal is recorded by the camera and analysed by an image analysis toolbox Andrea Alberti developed to calculate the atoms' position.

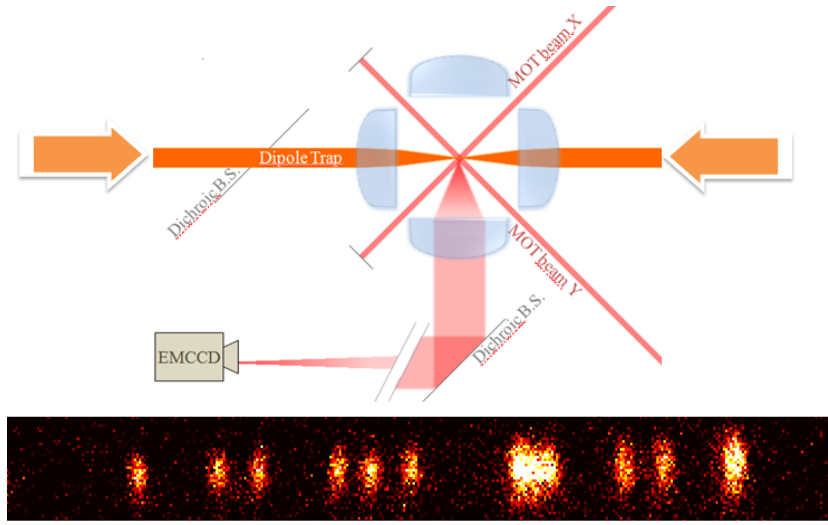


Figure 2.4: Imaging system. Top: Atoms are trapped in the dipole trap and illuminated by the MOT beams. The fluorescence is collected by one of the four lenses with a numerical aperture of 0.5. Image provided by Miguel Martinez Dorantes. Bottom: Typical emCCD image of trapped atoms. The FWHM of the LSF is around 3 pixels while one lattice site corresponds to 1.8 pixels. The brightest spot is caused by atoms in neighbouring lattice sites that cannot be resolved.

The toolbox reads in the two dimensional images the camera provides and sums over all pixels perpendicular to the trap to get a one dimensional intensity profile. In this profiles it defines regions of interests (ROIs) where the intensity profile is above a certain threshold. The resolution of the imaging system is larger than one lattice side. Therefore multiple atoms can be in the same ROI. With the total number of counts in a ROI its atom number is determined. From the signal of the single photon ROIs the Line Spread Function (LSF) is found experimentally. Using parametric deconvolution the position of the atoms is finally calculated below the diffraction limit.

The intensity of the dipole trap is smaller the farther away from the centre of the trap the atoms are. This results in a lower AC Stark shift that causes the detuning between the molasses beams and the transition to get lower the farther away from the centre of the trap the atom is positioned. Therefore atoms far away from the center of the trap appear brighter than atom at the center which has to be compensated for in the analysis of the images.

# Chapter 3

## Creation of a Dense Ensemble of Neutral Atoms

The aim of the experiment is the storage of a photon in an atomic ensemble inside of a fibre based optical cavity. The coupling between the atoms and the cavity is collectively enhanced by a factor of  $\sqrt{N}$  where  $N$  is the number of atoms inside of the cavity mode. Therefore, we need an atomic ensemble which is as dense as possible.

### 3.1 The Basic Principle

The basic principle of the compression follows the idea presented in [27]. At the beginning of the sequence, atoms are trapped in a standing wave dipole potential. By adiabatically lowering the intensity of one beam and simultaneously increasing the intensities of the other dipole trap arm the running wave potential is transformed into a running wave potential. It is important to do this adiabatically with respect to the oscillation frequency of the standing wave pattern to not heat the atoms.

In the standing wave potential the atoms are attracted to the centre of the trap and start to oscillate. The atom density is increased since the atoms are moving towards the centre. At the maximum density the potential is in the same manner adiabatically changed back into the standing wave potential with a high density at the centre of the trap. Figure 3.1 depicts this sequence.

To ensure that the potential is adiabatically changed the action has to remain invariant. This is strictly only true when  $\dot{\omega}/\omega^2 \rightarrow 0$ , e.g. the change of potential is infinitely slow [28]. Since we need to change the potential in finite time the change is not completely adiabatic. Therefore, the adiabaticity

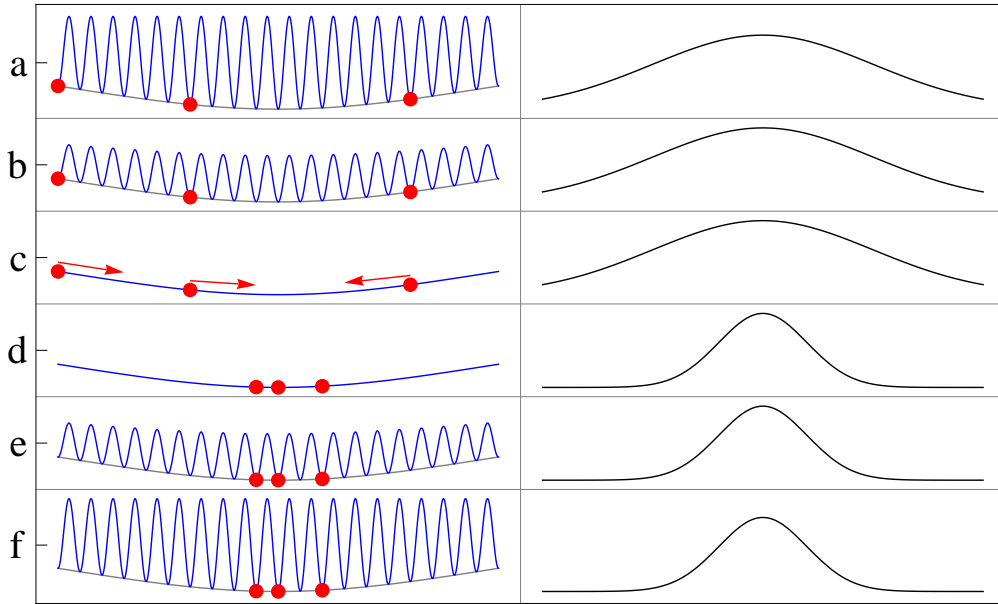


Figure 3.1: Illustration of the idealized compression sequence. Single atoms are trapped in a standing wave potential (a). Adiabatically the standing wave is changed to a running wave potential (b). Atoms start to oscillate (c). After a quarter oscillation period (d) the potential is changed back (e) to a standing wave potential (f). On the right the atom distribution is depicted.

parameter  $|\dot{\omega}/\omega^2|$  is kept much smaller than one by changing the potential slowly.

## 3.2 The Harmonic Approximation

The main step in the compression sequence is when the atoms follow the potential of a running wave dipole trap. Since a dipole trap causes a conservative potential the classical equation of motion is given by

$$m\ddot{\vec{r}} = -\nabla U(\vec{r}, t) \quad (3.1)$$

For atoms which are not positioned too far from the centre of the trap one can Taylor expand the potential up to the second order. Since the Rayleigh length

is about 90  $\mu\text{m}$  this is a good approximation for all atoms. The calculation can be found the appendix and results in formula A.2

$$U(\vec{x}) \approx U_0 \left( \frac{z^2}{z_R^2} + \frac{2\rho^2}{w_0^2} - 1 \right), \quad (3.2)$$

which also can be found in [29]. This leads to radial  $\omega_r$  and axial  $\omega_z$  oscillation frequencies of [29]

$$\omega_r = \sqrt{\frac{4U_0}{mw_0^2}} \quad (\approx 60000 \text{ s}^{-1}), \quad (3.3a)$$

$$\omega_z = \sqrt{\frac{2U_0}{mz_R^2}} \quad (\approx 5000 \text{ s}^{-1}). \quad (3.3b)$$

### 3.2.1 Compression in the Harmonic Approximation

In the harmonic approximation one can compute the atoms' behaviour analytically. This is interesting because one can directly see the dependences on the trap and the atoms initial condition. I neglect the effect of the radial oscillation and treat this as a one dimensional oscillation.

The loading is a random process and therefore we cannot control where the atoms are before the compression. But we can measure the initial distribution over many repetition which is approximately Gaussian with a width of  $\sigma_x$ . The centre of this distribution can be tuned to be at the centre of the trap. The atoms have an initial temperature. According to this temperature they move with a random velocity before the compression. In thermal equilibrium this velocity distribution is also Gaussian distributed [30].

With its initial position  $x_0$  and velocity  $v_0$  the atom performs harmonic oscillation according to

$$x(t) = x_0 \cos \omega_z t + \frac{v_0}{\omega_z} \sin \omega_z t. \quad (3.4)$$

The spatial standard deviation is defined as  $\sigma_x^2 = \langle x^2 \rangle - \langle x \rangle^2$ . But since  $\langle x \rangle = 0$  it simplifies to  $\sigma_x^2 = \langle x^2 \rangle$ . The spatial standard deviation as function of time

$$(\sigma_x(t))^2 = \cos^2(\omega t) \sigma_x^2 + \sin^2(\omega t) \frac{\sigma_v^2}{\omega^2} \quad (3.5)$$

is obtained in the appendix in formula A.3. The minimal possible spread of atoms is when  $\cos(\omega_z t) = 0$ , after a quarter oscillation period. In this case one obtains a minimal deviation of

$$\sigma_x^{\min} = \frac{\sigma_v}{\omega_z}. \quad (3.6)$$

This means that the compression is more effective the colder the atoms are. Additionally the higher the intensity of the trap the higher the oscillation frequency and therefore the higher the compression efficiency. A higher trap frequency can also be achieved through a shorter Rayleigh length.

### 3.3 The Experimental Realization

In the experiment we do not change the intensity of one arm but only the intensity of the other because we cannot put four times the original power into one arm. By this the trap depth of the resulting running wave potential has only a quarter of the trap depth of the standing wave trap depth. With the AOM we perform a sinusoidal ramp that has its minimum after 2 ms. After the atoms have been compressed the intensity is ramped up with the same ramp.

To improve the compression efficiency the compression sequence is repeated. The atoms are cooled in between each compression sequence. To characterize the compression sequence we use a sparsely loaded trap to do this. A high atomic density lead to a high probability that atoms share a lattice site. Those atoms would be lost due to light assisted collision [31] in the imaging process. If we use the compression sequence to have as many atoms as possible inside the cavity mode volume we would of course use a dense loading of the dipole trap.

An additional advantage of the sparse loading is that it is easier to extract the atom number from the images

After we loaded the dipole trap we take a first image. Afterwards we start the compression sequence and image the atoms again. Here, this is repeated five times. The camera gives a two dimensional image of the atoms in the dipole trap. By summing over all pixels perpendicular to the dipole trap we get a one dimensional intensity profile of the atoms. To increase the statistics we repeat the experiment with the same settings. In figure 3.2 one can see the averaged intensity profiles of 500 individual trials. Those contain the fluorescence of 1000-1500 loaded atoms. If the compression is successful there is an intensity peak around the centre of the trap.

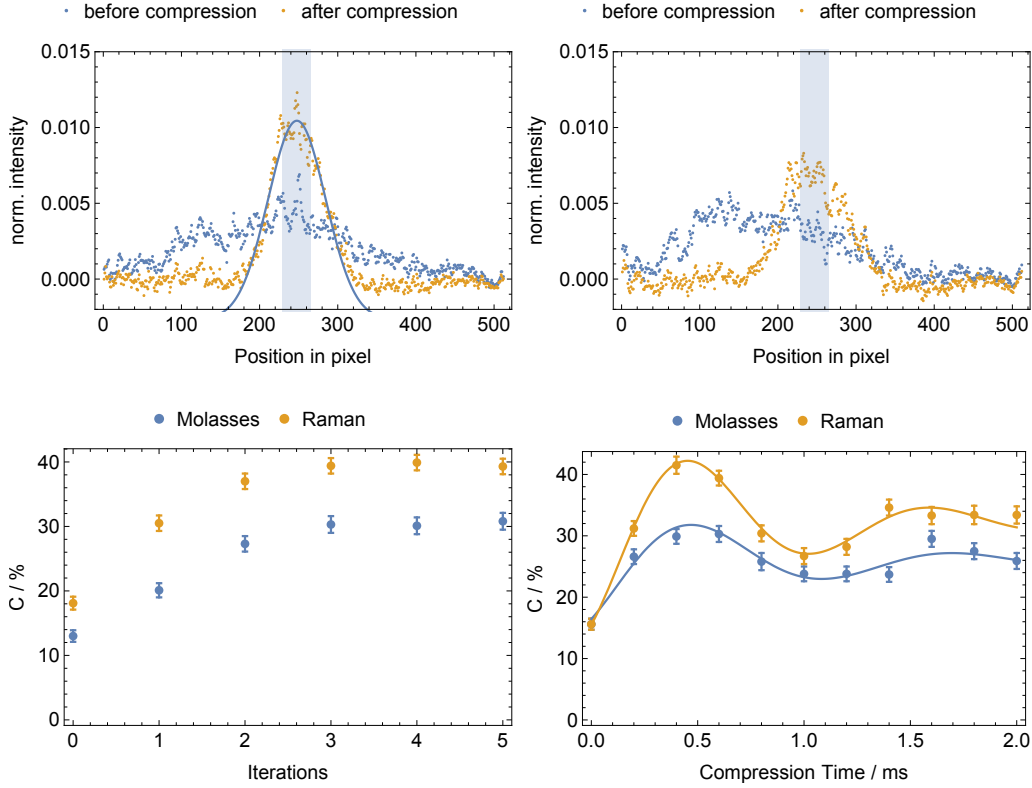


Figure 3.2: Top: Averaged intensity profile before the compression (blue dots) and after 3 compression sequences of 0.6 ms (orange dots) of Raman cooled (left) and Molasses cooled atoms (right). The shaded area marks the cavity volume. Additional Gaussian fit to find the centre of the trap (left). Bottom: Compression rate versus the repetition number (left, 0.4 ms compression time) and the versus the compression time (right).

In the compression sequence the atoms are compressed at the centre of the trap. Since the cavity will be placed at the centre of the trap it is very important to know the centre of the trap. To get this we need the atoms' positions after a successful compression. I define the mean of those positions as the centre.

In the top left plot in figure 3.2 we have also fitted Gaussian to the intensity peak and thereby determined the centre of the trap. The centre positions found by this two methods differ less than one pixel. The shown intensity profile was obtained by three consecutive compressions of Raman cooled atoms with 0.6 ms compression time.

The width of the this Gaussian fit is 36 pixels. This corresponds to 20 lattice

sites which are roughly  $9\ \mu\text{m}$ . Raman cooled atoms have a temperature of around  $1\ \mu\text{K}$  [32]. For a compression with our parameters and a temperature of  $1\ \mu\text{K}$  formula 3.4 predicts a width of only  $2\ \mu\text{m}$ .

The top right image shows that atoms which are only cooled with the molasses and not with Raman cooling cause a broader intensity profile. Without Raman cooling the atoms temperature of the atoms is around  $50\ \mu\text{K}$  [32]. Formula 3.4 suggest a width of  $14\ \mu\text{m}$  for the compressed ensemble. A fit to the data shown in figure 3.2 one finds a width of around  $12\ \mu\text{m}$  which is very near to the predicted value.

The waist of the cavity mode will be around 10 lattice side which are roughly 18 pixels. We define the compression rate  $C$  as the fraction of loaded atoms inside this mode volume. There are only two possibilities. Either the atom is inside the cavity mode volume or not. The inaccuracy of the measurement can therefore be given by the binomial error [33]

$$\Delta C = \sqrt{\frac{C(1-C)}{N}}, \quad (3.7)$$

where  $N$  is the number of loaded atoms. The bottom left image shows the compression rate versus the number of compression sequences with a compression time of  $0.4\ \text{ms}$ . The compression rate does not change after three compression sequences. Therefore we used three sequences to compress the atoms.

The bottom right plot of figure 3.2 shows the compression rate versus the compression time. For a perfectly harmonic trap one would expect a sinusoidal dependence. The asymmetry of the trap leads to a damping of the sinusoidal curve. The fitted curves assumed the damping to be exponential. The same kind of damping was observed in [27]. Raman increases the compression rate to 40 %.

### 3.4 The Simulation

I analysed the complete behaviour of the atoms in the compression sequence with a Monte Carlo simulation<sup>1</sup>. In addition to the analytic treatment in the harmonic approximation the simulation includes the asymmetry of the trap and the three dimensional motion of the atoms. The atomic motion is still classical.

For every atom random starting values for position and velocity are assigned.

---

<sup>1</sup>For this I extended a one dimensional simulation Lothar Ratschbacher wrote in mathematica.

Afterwards the equation of motion is solved for the atoms independently over the whole time of the compression sequence. After the compression time the movement of the atom is calculated for some additional time. Atoms could gain so much energy that they are not trapped any more but are still positioned within the cavity volume. Those atom leave the cavity volume during the additional time.

The starting value for the velocity are Gaussian distributed according to their temperature. In thermal equilibrium the standard deviation of the velocity distribution is given by [30]

$$\sigma_v = \sqrt{\frac{m}{k_B T}}, \quad (3.8)$$

with the Boltzmann constant  $k_B$ . Analogous to chapter 3.2.1 the overall distribution is Gaussian. In the beginning there is a standing wave. Therefore, the atoms' position is always near the potential minimum. Because of this, the Gaussian distribution is discretized. Inside of the lattice sides the spatial distribution is according to the temperature Gaussian distributed with a sigma of

$$\sigma_{LS} = \frac{\sigma_v}{\omega}, \quad (3.9)$$

where  $\omega$  is the radial or axial standing wave trap frequency respectively. The movement of the atoms is considered to be completely classical. The equation of motion is therefore given by formula 3.1. The potential of 2 counter propagating beams is given by

$$U(\vec{x}, t) = 4U_2(t)U_{sw}(\vec{x}) + (U_1(t) - U_2(t))U_{rw}(\vec{x}), \quad (3.10)$$

where  $U_1(t)$  is the trap depth a running wave trap with the intensity of the stronger beam would have and  $U_2(t)$  the one with the intensity of the weaker beam.  $U_{sw}$  and  $U_{rw}$  give the form of a running or standing wave potential that are defined in formulae 2.7 and 2.6. The intensities change in time to perform the compression sequence. We can now consider different ramping scenarios to study the performance of the compression sequence. The first ramping type I will call adiabatic ramp since it keeps the adiabaticity parameter constant. For this the intensity of one arm is ramped down according to

$$U_2(t) \propto \frac{1}{1 + \Gamma t}, \quad (3.11)$$

where  $\Gamma$  gives the speed of the ramping process. After the ramping time is over  $U_2(t)$  is set to almost zero. After a quarter oscillation the ramping up process begins, where the intensity follows as

$$U_2(t) \propto \frac{1}{1 + \Gamma(T - t)}. \quad (3.12)$$

In the whole sequence the overall depth of the potential is kept constant. For this purpose the other arm has to be ramped according to

$$U_1(t) = \left(2\sqrt{U_2(0)} - \sqrt{U_2(t)}\right)^2. \quad (3.13)$$

The same ramping type is used in [27]. In the experiment we do not use this ramp but a sinusoidal ramp. The sinusoidal ramp has only one parameter. The speed of the ramp down is just given by the length of the ramp. It is therefore much easier to find the optimal parameters.

The movement of the atom is simulated according to formula 3.10 and the position of the atom is monitored at the end of the sequence. The interesting figure of merit is again the fraction of atoms inside of the cavity mode  $C$ .

Figure 3.3 shows the evolution of spatial distribution of atoms in the compression sequence. On the top left one can see the an example trajectory of a single simulated atom. In the beginning this atom is trapped in one lattice side (here -12) and performing oscillations. When the running wave potential is lowered, the amplitude and the period of the oscillation is increased are. When the intensity of one beam is turned off the atom is moving towards the centre of the trap. After the standing wave potential is turned on again the atom is trapped in lattice side -1. The vertical lines mark the start and the end of the quarter oscillation period where the compression takes place. The oscillations the atom performs in the last part of the simulation have a higher amplitude since the atom gained energy in the process.

On the top right side of figure 3.3 the spatial distribution of atoms before the compression sequence is shown. Only few atom are positioned inside of the mode volume (highlighted region). After a quarter oscillation period but before the standing wave potential is ramped up again the peak density is highest (bottom left). Note that since we do not have the altering potential any more the atoms are not confined to lattice sites and the atoms can be at intermediate position. The histogram therefore shows the intermediate position which results in more bars. Next to this there is the histogram of the final spatial distribution. The atoms are again confined in lattice sites. According to the experimental data an additional compression step leads to a

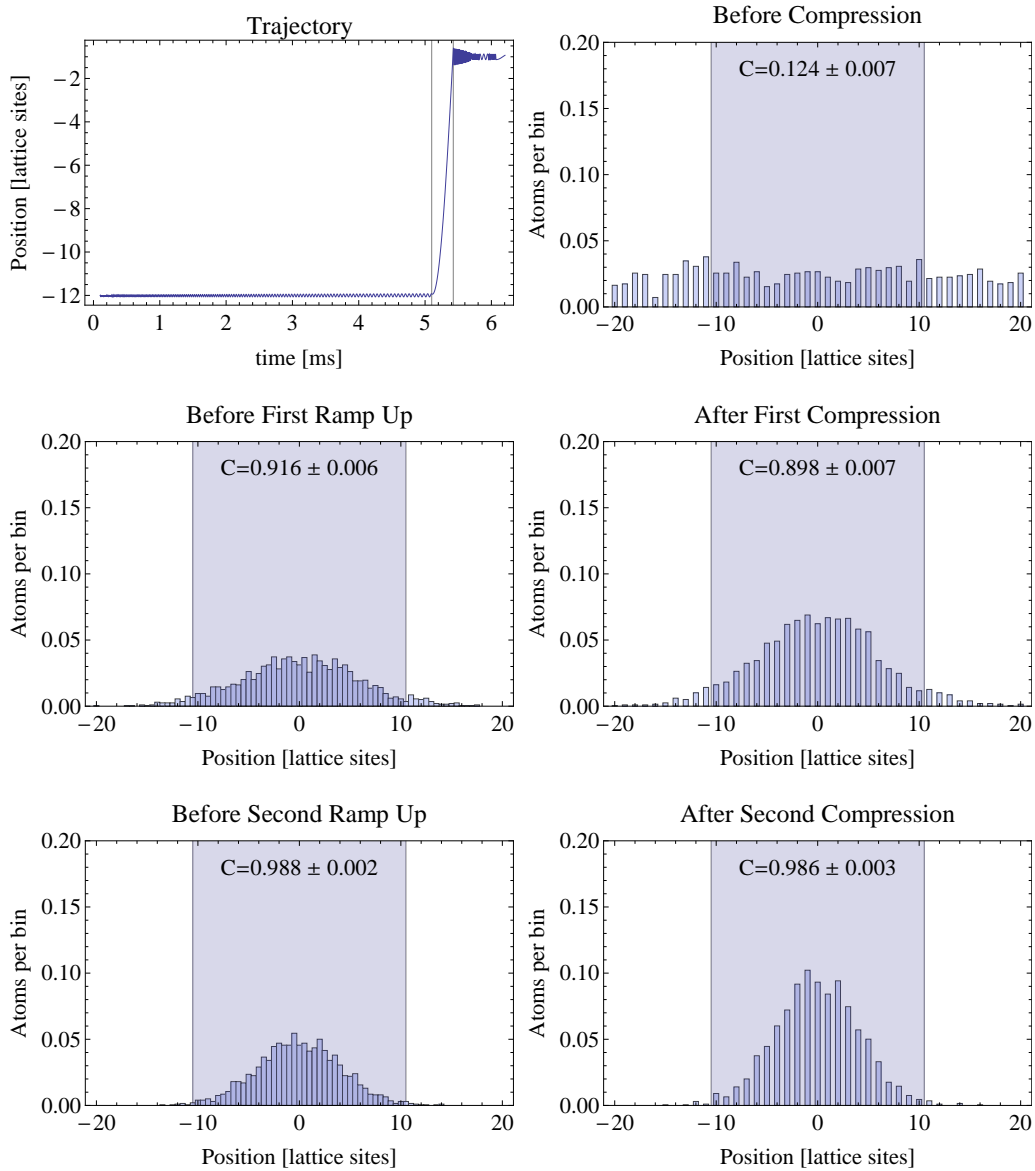


Figure 3.3: Top left: Trajectory of a single atom in the compression sequence. Top right: Spatial distribution of atoms before the compression sequence obtained with 2000 atoms. Middle left: Spatial distribution of atoms after a quarter oscillation period. Middle right: final spatial distribution of atoms after one compression. Bottom: The distribution in a second compression sequence.

further increase of  $C$ . The histograms shown at the bottom of figure 3.3 show that this is also true for the simulated compression. This can be explained due to the anharmonic trap. For a perfectly harmonic trap all atoms have the same oscillation frequency, whereas this is not true for an inharmonic trap. The outer atoms have a longer oscillation frequency in the trap and are therefore not perfectly compressed. In the second sequence they start near the centre and where the trap is nearly harmonic. Therefore those atoms are compressed with the maximal possible efficiency.

The simulated compression leads to a higher compression rate than the experimental data. This is again due to the fact that classical motion is not a good treatment for atoms cooled to the quantum mechanical ground state. Optimal control algorithms could lead to a better agreement with the experiment and can therefore be used to optimize the compression process further. This simulation was made with the adiabatic ramp, a trap depth of 0.25 mK and 2000 simulated atoms with an initial temperature of 1  $\mu$ K.

### 3.5 Crossed Beam Compression

As explained in chapter 3.2.1 the efficiency of the compression depends on the trap frequency. One way to strongly increase the trap frequency is to introduce a running wave potential perpendicular to the trap. Because of a lack of analogue channels for the experimental control this was not implemented in the current setup. In near future the experimental control will be exchanged and then this can be experimentally realized.

The potential depicted in figure 3.4 is the potential of two running wave dipole traps that crosses each other perpendicularly at their centre. In a compression with additional potential this perpendicular running wave dipole trap beam remains unchanged in the whole compression sequence. The sequence of the original two beams is the very same as before. The only difference is that the compression time has to be adapted because of the higher oscillation frequency.

A requirement for a successful compression is that all atoms reach the centre of the trap in roughly the same time. For this, the potential has to be nearly harmonic. The potential depicted in figure 3.4 is not harmonic. If the atoms are compressed before they are near the centre and within the waist of the crossed running wave dipole trap the potential can be approximated by a harmonic one. Therefore this compression has to be a two step compression. The first step is without the additional compression and the second one with. Figure 3.5 shows the compression efficiency in this scheme. Although  $C$  is not increased in the second compression but slightly lowered one can see a

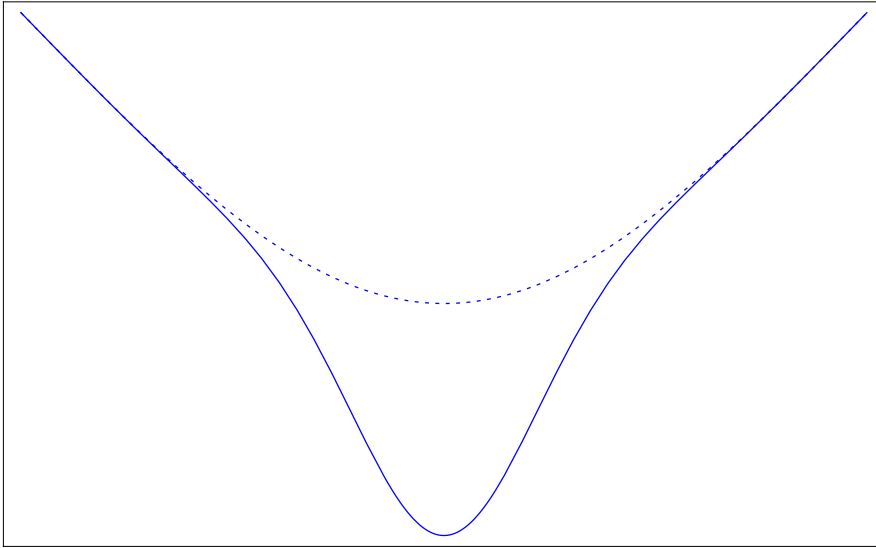


Figure 3.4: The potential of two crossed running wave dipole traps (solid line). The dotted line represents the potential of a single running wave potential.

much higher filling of the central lattice sites. The shape of the distribution changes. While the distribution of atoms after the first compression looks Gaussian it is clearly non-Gaussian after the second compression. This is due to the strongly anharmonic trap. Because of the higher filling of the central lattice sites the two dimensional compression would be less effected by changes in the position of the trap.

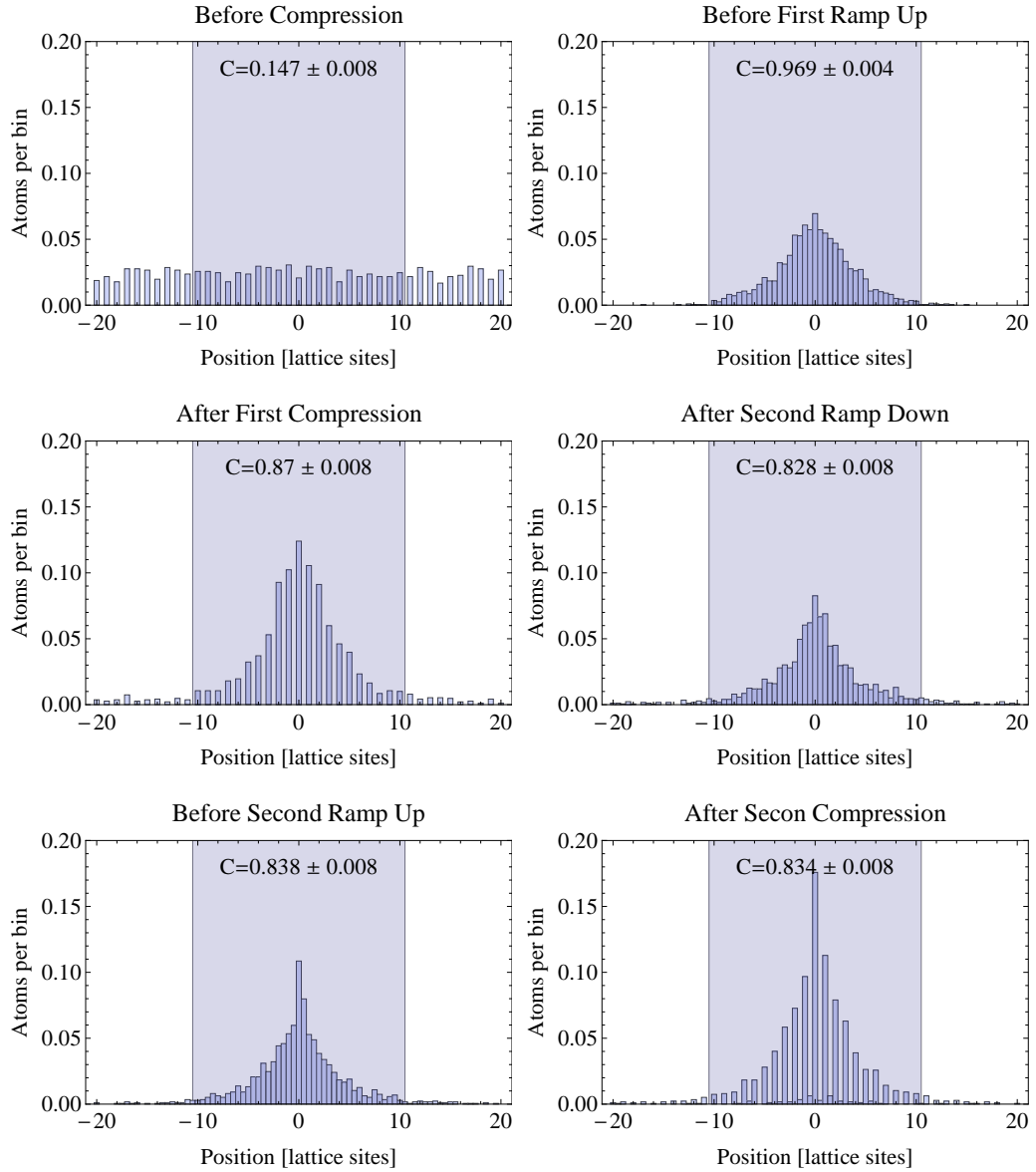


Figure 3.5: Simulated spatial distribution of atoms in the crossed beam compression sequence at six different times. The shaded area represent the cavity mode volume. This was made with 2000 simulated atoms and a trap depth of 1 mK.

# Chapter 4

## Non-Destructive Free Space Hyperfine State Detection

Every experiment which uses qubits needs a method to read out the qubit information. Since we are using the hyperfine ground state of Rubidium in the experiment we need a method to distinguish between both hyperfine states. A standard method for trapped neutral atoms is the so called push out technique which has been used in our group for several years now [34]. A strong resonant laser pushes out atoms in one hyperfine state but not in the other. This is destructive in the sense that atoms cannot be used in multiple measurements and the dipole trap has to be reloaded.

For trapped ions the trap is usually several 1000 K deep. Therefore ions cannot be pushed out of their trap using laser light. The standard method there is to use the different fluorescence signals of the ion states to distinguish between them [35, 36]. Here one state acts as the bright state which emits photons and the other state of the qubit act as a dark state which does not emit any photons. From the collected photons the ion state can be inferred. The detection error of method has been shown to be below  $10^{-3}$  [36] for multiple atoms observed with a camera.

A non-destructive state detection for neutral atoms using there fluorescence signal has been realised with a 2 % error using an optical tweezer [18] and 5 % using a standing wave dipole trap [19]. All those measurements were done with individual atoms and a single photon counter. Here, we demonstrate the simultaneous non-destructive state detection for neutral atoms using a CCD camera.

In all non-destructive methods there is still a certain probability to lose the atom. Therefore there are two different important figures of merit. The first one is the survival probability, which is the probability that an atom is still trapped after it is imaged consecutively in the both hyperfine states. In an

ideal push out scheme this is 0 since all the atoms are lost while imaged in one hyperfine state. In an ideal non-destructive method this is 1. Here we are interested in a survival probability of above 0.95. The other important figure of merit is the detection error which is the fraction of wrongly detected atoms in a single shot experiment.

Fast non-destructive state detection of neutral atoms is also possible inside an optical cavity [12] but this method cannot be applied for multiple atoms simultaneously.

To do non-destructive state detection simultaneously for multiple atoms one has to use a camera. There is an intrinsic trade off between spatial resolution and state detection fidelity. If the light would be focussed on a single pixel the noise of the detected signal is lowest. But there would be no way to tell which signal comes from which atom. For this reason it is more difficult to do the state detection with multiple atoms.

## 4.1 State Dependent Imaging

For state dependent imaging one needs a transition where atoms in one hyperfine ground state scatter photons and atoms in the other do not. Since the atoms shall scatter as many photons as possible we use a cyclic transition where the atom can only fall back in its original state after one absorption-emission cycle.

There are two different cyclic transitions available if the D2 line is used. Either we use the  $F = 1 \rightarrow F' = 0$  or the  $F = 2 \rightarrow F' = 3$  transition. In the same manner as explained in chapter 2.2 off resonant excitation will occur. The longer the atoms stay on the cyclic transition the more photons they emit. Using the outermost Zeeman sublevels one can suppress off resonant excitation not only by frequency but also by polarization. We therefore choose the  $F = 2 \rightarrow F' = 3$  transition. The atom is illuminated with circular polarized light along the quantization axis which is defined by a magnetic field generated by the same coils that create the MOT field.

The  $F = 1$  state will be referred to as the dark state since atoms in this state will not scatter photons. Atoms in the  $F = 2$  state will scatter photons and therefore I will refer to them as bright atoms. Figure 4.1 depicts this state depending imaging transitions. In all measurements presented here the atoms are imaged for 5 ms.

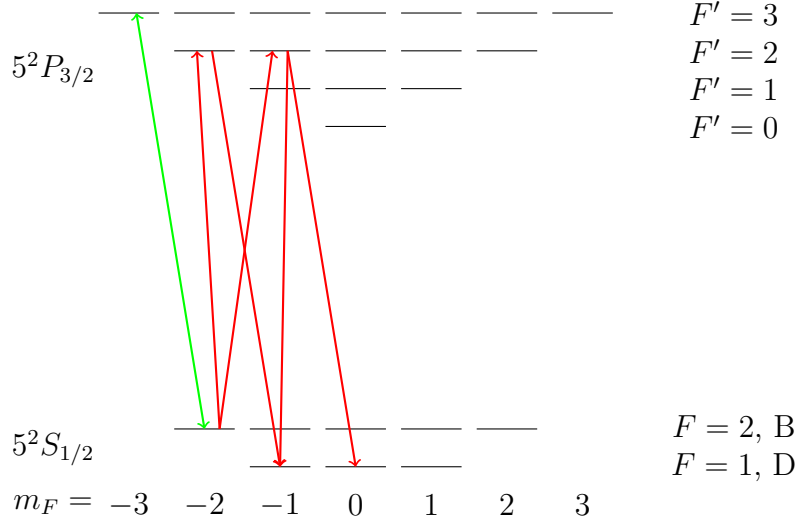


Figure 4.1: Level structure of the Rubidium 87  $D_2$  line. In green: the cyclic transition used for state dependent imaging. In red: dominant leakage paths to the dark state

## 4.2 The Detection Error

Based on the on the photon record the most likely state of an atom is inferred. A certain criterion is applied to a photon record in order to make the state detection decision. This criterion is not perfect. The detection error  $\epsilon$  is the fraction of atoms that are wrongly detected in a single shot measurement.

In the simplest case this criterion is a threshold. If the record is higher than this threshold the atom is considered bright and if not it is considered dark. If the fluorescence signal of an atom is above this threshold it is considered to be bright, otherwise it is considered dark. Since this two distributions will overlap some of the dark atoms will considered bright and vice versa.

We define the the bright state error  $\epsilon_B(T)$  as the fraction of bright atoms that are wrongly detected as dark ones and the dark state error  $\epsilon_D(T)$  as the fraction of dark atoms that are wrongly detected. The mean error  $\epsilon_{\text{mean}}(T)$  is defined of the mean of this two errors.

In figure 4.2 this is depicted. The blue shaded area gives the  $\epsilon_B$  and the red shaded area gives  $\epsilon_D$ .

All those errors depend on the threshold position  $T$ . A scan of possible threshold positions lead to a minimal mean error which we define as the detection error  $\epsilon$ . This method is very commonly used [18, 19, 35]

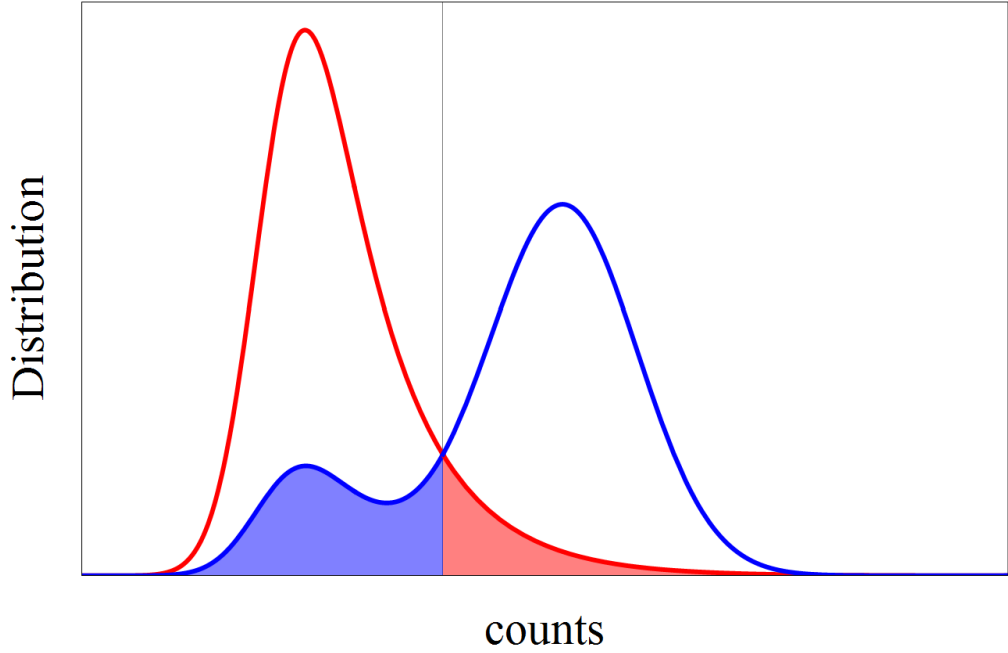


Figure 4.2: Exemplary distribution of counts for bright atoms (blue curve) and dark atoms (red curve). The grey line depicts the threshold. Bright atoms with their fluorescence signal in the blue shaded area are wrongly detected. The same is true for dark atoms in the red shaded area.

### 4.3 Experimental Sequence and Analysis Program

To measure the detection error and the survival probability for given imaging conditions we use a test sequence. The first step in this sequence is of course loading the dipole trap. To have mostly separated atoms we load the dipole trap sparsely. To ensure that the Stark shift does not lead to different transition frequencies for different atoms we compress the atoms.

The detection error is the mean of the fraction of wrongly detected bright and dark atoms. To calculate this we need to image atoms in the dark and in the bright state independently. After loading the dipole trap and compress the atoms we take a state independent image. Afterwards we pump the atoms in the dark state and take a state dependent image. This is repeated with the bright state. To check which atoms have survived the imaging process an additional state independent image is taken. In principle with this sequence we measure the detection error plus the preparation error. With traditional

push out method we checked that the preparation can be neglected compared to the detection error. This sequence is repeated 100 times before the dipole trap is reloaded. Figure 4.3 the images taken in one of this sequences.

With help of the image analysis toolbox Andrea Alberti developed I wrote a program that calculates the detection error and the survival probability. In a first step the program fits the position of all individual atoms. If the positions of one atom differs less than one pixel in both state independent images the atom must have survived the imaging process. The survival probability directly follows from the fraction of atom that survived. We postselect the data of survived atoms.

We define a region of interest (ROI) for each atom. This ROI consists of the pixel at the fitted position of the atom and two additional pixels to the right and left of this central pixel. We measure the integrated counts inside this ROI for the state dependent images for the dark state and the bright state individually. By doing this for all atoms a histogram of those integrated counts gives the desired distributions. The distribution measured for a given set of imaging conditions are shown in figure 4.4. From those distributions the detection error can be extracted.

The survival probability  $S$  is the fraction of survived atoms. Since this is a binary information, either the atom has survived or the atom has not, the statistical error of the survival probability can be given as the binomial error [33]

$$\Delta S = \sqrt{\frac{S(1-S)}{N}}, \quad (4.1)$$

where  $N$  is the sample size which mean here the number of detected atoms. The error calculation of the detection error is more complicated and has to be calculated with a bootstrap algorithm.

The detection error is calculated from a sample of  $N$  measured atoms. From this sample  $k$  subsamples of the same size are created. Each element of this subsamples is a randomly chosen measured atom. The same atom can be chosen multiple times within one subsamples. The detection error is now calculated from every subsample and by this a distribution of detection error is created.

Following [37] the margin of error is defined as the 16 % and the 84 % quartile. This gives a hint how to choose  $k$ . The the margin of error converges and therefore  $k$  has to be large enough that the margin of error does not change significantly when more subsamples are considered.

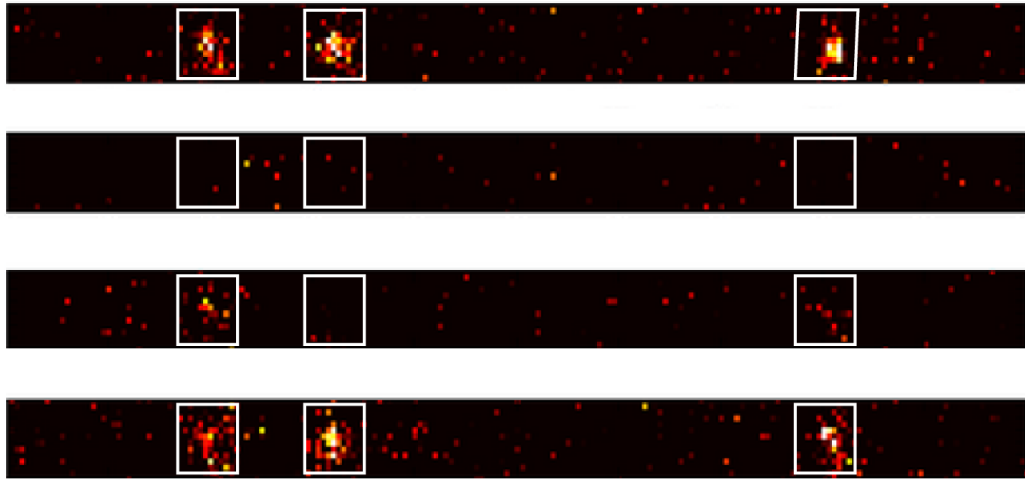


Figure 4.3: Schematic depiction of the test sequence. Top: State independent image of three atoms. The position can be calculate and a ROI (white boxes) can be found. Afterwards the atoms are pumped in the dark state and a SD image is taken (second image) before the atoms are pumped in the bright state and a second SD images is taken (third image). With an additional state independent image the survival of the atom is checked. This additional normal image also works as the first image of the following sequence.

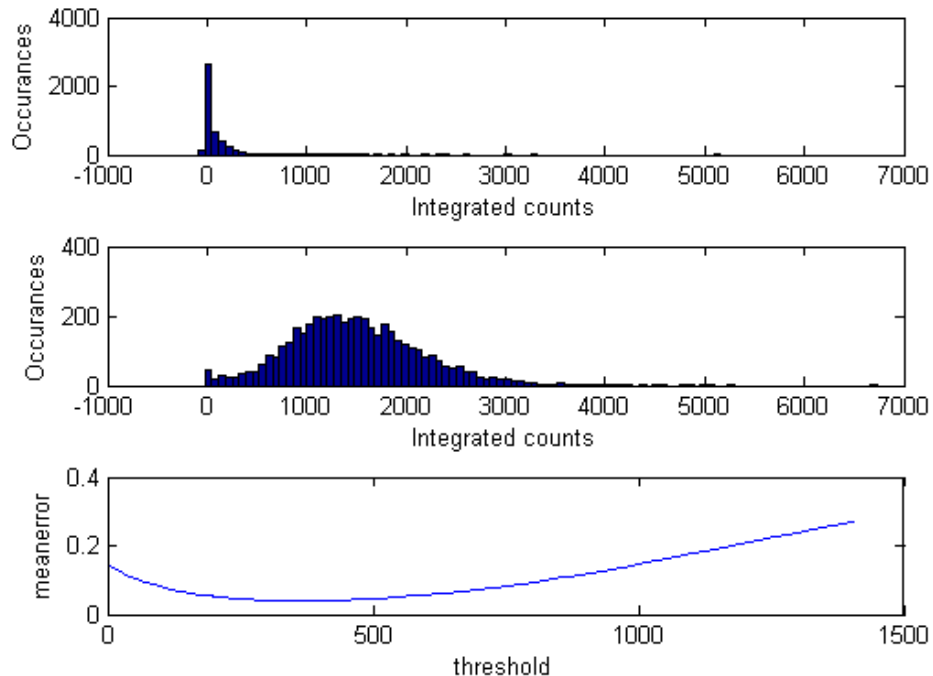


Figure 4.4: Example of the detection error estimation. Top: a histogram of measured dark state integrated counts. Middle: the same for the bright state. Bottom: the mean error for a big set of possible thresholds with a minimum of 4.05 %

## 4.4 The Camera

In the experiment we focus the fluorescence light of the atoms onto an emCCD camera to observe the atoms. In this section I will explain the camera. This camera is the main information source of the system. The camera is an imperfect detector. We need to have a understanding of the camera in order to theoretically study different imaging parameter regimes and optimize the state detection.

### 4.4.1 Working Principle

Figure 4.5 shows the working principle of an emCCD camera which is identical to the one of a conventional CCD but with an additional gain register. Photons hit the active area of the CCD creating electron hole pairs on the individual pixels. The charge created by the photoelectrons is accumulated on the individual pixel during the imaging time. After the exposure the electrons are shifted vertically. This happens by changing the electric potentials and move the electrons to the position of the next pixel. By this the photoelectrons of one row of pixels reach the readout register.

In a normal CCD those pixels would be horizontally shifted and electronically read out. In an emCCD the electrons are horizontally shifted in a multiplication stage. The shift in the gain register works similar to the previous shift but the potential of the neighbouring stage is much steeper than before. Therefore, the electrons gain momentum and can cause impact ionization which creates an additional electron hole pair. The probability that this happens is quite low (around 1 % per electron per stage [38]) but since there are couple of hundred those stages [38], a gain of factor of several  $10^3$  can be achieved. This electron multiplied signal is then electronically read out.

After the complete row of pixels is read out, a new row of pixels are shifted vertically into the read out register and the multiplication procedure starts again.

### 4.4.2 Important Functions

There are multiple settings the camera software provides that can be modified in order to get an optimal signal to noise ratio. I will briefly explain the most important ones.

**Baseline clipping:** There is a certain offset in counts for every single pixel. Baseline Clipping ensures that this offset (baseline) stays at 100 counts for

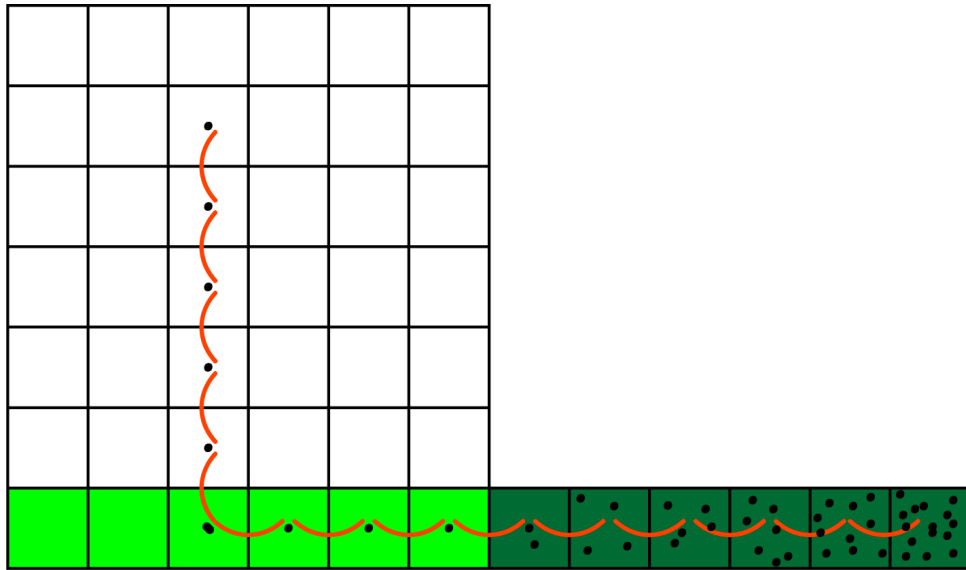


Figure 4.5: Working principle of an emCCD camera. A photon hits the active area of the camera and a electron hole pair is created. The electron (black dot) is kept in a electric potential which forms a pixel. When the image is read out the electron is (vertically) shifted into the read out register (light green boxes). Afterwards the photoelectron is shifted in the gain register (dark green boxes where it is multiplied). The electronic read out of this gives a count for every single pixel. Note that the efficiency of electron multiplication is strongly exaggerated

all pixels. This is done by subtracting an average bias for each pixel [38].

**Read out speed:** The read out speed gives the shifting rate. The higher this rate the faster the readout. For faster read out Clock Induced Charges (see chapter 4.4.3) are less probable [38].

**EM gain level:** The higher the EM gain level the higher the counts per photon. This increases the signal to noise ratio. High gain level lead to an ageing effect of the camera which lowers the effective gain with time [38].

**Clock Amplitude:** A high Clock amplitude enables even faster readout and charge leakage to neighbouring pixels gets suppressed [38]. A high amplitude also leads to more Clock Induced Charges [38]( see section 4.4).

### 4.4.3 Camera Noise

It is important to understand the noise sources of the camera. In the state detection images the signal to noise ratio is one of the limitation.

#### Noise sources

The camera noise can be generated at different stages.

**Read out noise:** Noise that is generated by the electronic read out [25].

**Clock Induced Charges (CIC):** Electron hole pairs which are generated in the shifting process. Those are amplified in the whole amplification stage and therefore indistinguishable from real photons [25].

**serial Clock Induced Charges (sCIC):** CIC generated in the amplification stage. They are therefore not amplified by the entire magnification stage and lead to less counts than CIC [39].

**Dark Current:** Thermally generated electron hole pairs in the substrate of the CCD chip while exposure. The amount of electrons which are accumulated is proportional to the exposure time [25]. Since we operate the camera with a temperature of  $-90^{\circ}\text{C}$  and have very short exposure times noise due to dark current can be neglected.

**Photo-response non-uniformity:** The noise due to variations in the photon response of the individual pixels, which can be caused by imperfect material or geometry of the pixels [25].

#### Noise Characterization

To characterize the noise of the camera we took images with a closed shutter. Figure 4.6 shows a histogram of pixel counts obtained by in this way. I will refer to this as a noise spectrum. The data was obtained by using maximum gain of 1000. Around  $10^7$  individual pixels contribute to this.

If no electron hole pairs are created due to dark current or CIC the electronic read out is the only noise contribution and one would expect a Gaussian noise spectrum. Indeed, one can find a Gaussian peak in the noise spectrum.

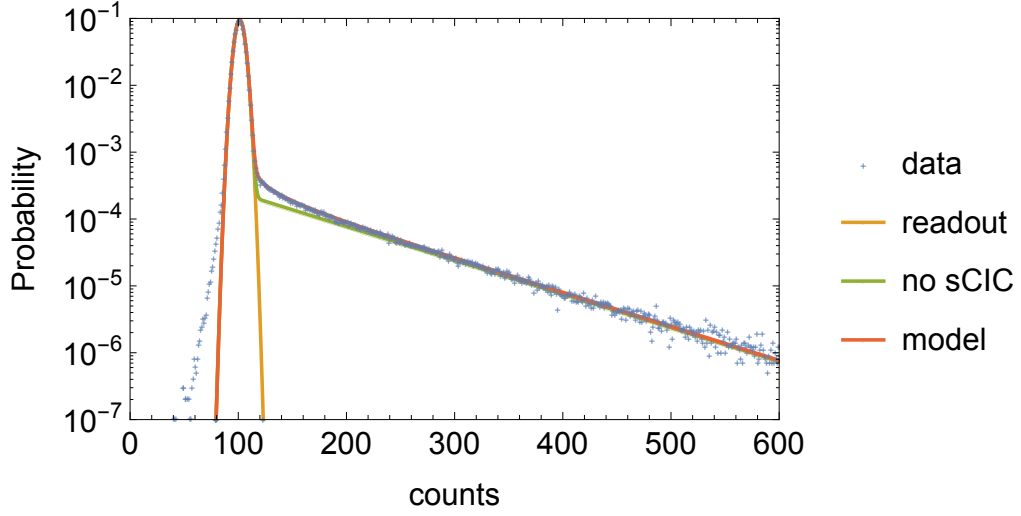


Figure 4.6: Camera Noise Spectrum

The yellow line in figure 4.6 shows a Gaussian fit to the the data. The corresponding noise distribution is

$$D_{\text{read}}(c, \mu, \sigma) = \frac{1}{2\pi\sigma} \exp\left(-\frac{(c - \mu)^2}{2\sigma^2}\right), \quad (4.2)$$

with the offset  $\mu$  and the width  $\sigma$ . Towards higher counts the noise spectrum is exponential. This is due to photoelectrons. In literature one finds that the counts of a photoelectron are exponentially distributed [39, 40]. Those photoelectrons are either CIC or generated by dark current. The green line in the figure 4.6 shows the distribution of counts for the read out noise and the contribution of one photoelectron. Since the probability of a photoelectron for a dark image exposure is quite low I neglect the possibility of getting multiple photoelectrons per pixel here. The exponential distribution of EM multiplied electrons needs to be convoluted with the Gaussian electronic read out noise. The one distribution of counts for a single pixel that has recorded one photoelectron is given by

$$D_1(c, \mu, \sigma, \lambda) = \Theta(c) \frac{e^{-\lambda c}}{\lambda} D_{\text{read}}(c) \quad (4.3a)$$

$$= \frac{\lambda}{2} e^{\frac{1}{2}(-2c + 2\mu + \lambda\sigma^2)} \lambda \text{erfc}\left(\frac{-x + \mu + \lambda\sigma^2}{\sqrt{2}\sigma}\right), \quad (4.3b)$$

where  $\text{erfc}(c) = 2\pi^{-0.5} \int_c^\infty dx \exp(-x^2)$  is the complementary error function,  $\Theta(c)$  is the Heavyside step function and  $\lambda^{-1}$  is the mean number of counts per photon.

Figure 4.6 also shows that in the regime where the exponential takes over to be the dominant part of the spectrum the green line differs from the data. This is because of sCIC. Since the sCIC are produced later in the multiplication stage they are amplified less. The mean number of counts per sCIC therefore depends on the stage where the sCIC is created. Following [39] the mean number of counts for a sCIC created in the  $i$ -th of  $N_{\text{stage}}$  amplification stage is given by  $1/\lambda' = \lambda^{-i/N_{\text{stages}}}$ .

With this three contributions the noise function can be written as

$$N(c) = aD_1(c, \mu, \sigma, \lambda) + bD_{\text{sCIC}}(c, \mu, \sigma, \lambda) + (1 - a - b)D_{\text{read}}(c, \mu, \sigma) \quad (4.4)$$

The orange line in figure 4.6 shows the best fit for this model.

For very low count rates the red line differs from the data. This is due to a change in offset. If one does not use baseline clamping this effect is much bigger. It seems like baseline clamping does not work perfectly.

### Noise Dependence on the Trigger Modes

In the experiment we observed that the camera noise differs with the trigger mode. There are three different modes available.

**External trigger:** The camera takes takes an image every time a hardware TTL trigger is send. This would be the obvious choice for any kind of sequence since there is no synchronizing between the camera and the sequence necessary.

**External start:** Here the camera waits for a trigger and then takes images in predefined time steps. After all images of one file are taken the camera waits for a new trigger to begin the next file. In this mode it is necessary to synchronize the sequence and the timing of the images within one file.

**Internal trigger.** After the camera is initialized no trigger is used for the timing of the images. When started the images are taken in predefined time steps the in the same way as in the external start mode. After the images of one file are taken, a new file automatically starts. In this mode it is impossible to synchronize an experimental sequence and the camera because not only the time within the sequence has to be be matched but also the overall of the sequence. Normally, the sequences are repeated hundreds or

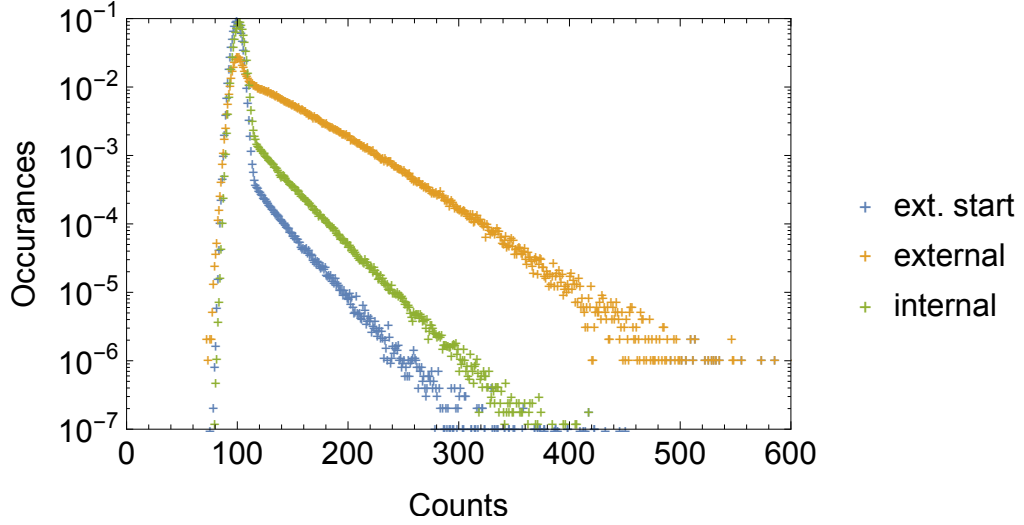


Figure 4.7: Noise spectrum of images taken with closed shutter using different trigger modes. All images were taken with an EM gain of 300.

even thousands of times.

Figure 4.7 shows the noise spectra of different trigger modes. On first sight one can see the difference in the probability of getting a photoelectron. With the external start mode (blue curve) one gets by far the lowest probability (around 1.1%). By using the internal trigger (green curve) this increases to around 5.9%. When the external trigger is used the shape of the noise spectrum changes. There are so many photoelectrons that the two photoelectron distribution has a significant impact on the noise which, therefore, cannot be described by formula 4.4.

For the state detection as well as for every other kind of measurement we want to have a signal to noise ratio which is as good as possible therefore the external triggering is not an option. Therefore much effort has to be put in the synchronizing between the camera timing and the experimental sequence. The same conclusion was found in [36].

It is not clear why the trigger modes lead to different results. This may have something to do with clearing the charges from prior exposures.

### Binning of pixels

When we image a single atom the fluorescence light hits multiple pixels and we collect the counts in a region of interest (ROI). We can do this in two

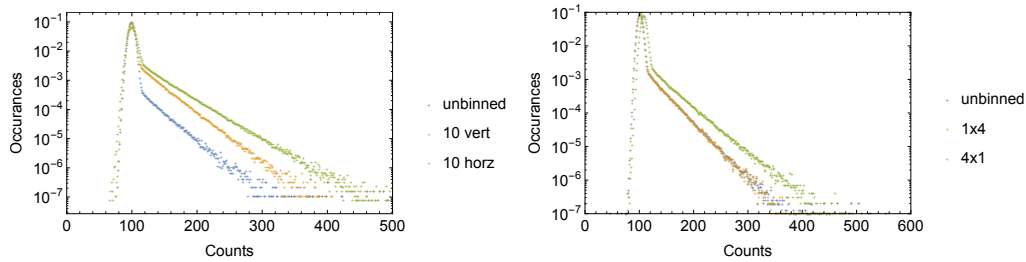


Figure 4.8: Left: Noise spectrum for different binnings using external start. Right: using internal trigger

possible ways. Either we read out every pixel individually and add the counts afterwards, which I will call software binning, or we use hardware binning. The latter means that the photoelectrons of several pixels are merged together on the CCD chip before the read out. It is important to differentiate between vertical binning and horizontal binning.

Vertical binning means that the binning is performed parallel to the first shift direction and horizontal binning means that the binning is performed perpendicular to this.

Since the camera noise differs for the possible trigger modes it I will compare the binning for all trigger modes individually.

Figure 4.8 shows the camera noise spectrum when hardware binning is used. The top image shows data taken with the external start mode.

The noise spectrum when vertical binning is used (orange) looks like the single pixel noise spectrum (blue) with an increased photoelectron rate. There is a clear difference between the horizontal (green) binning and the vertical binning. In the horizontal binning mode more photoelectrons are created. With the naked eye one can see a difference in the slope of the exponential tail. Obviously the binning has an effect on the gain.

The right image shows the behaviour when internal binning is used. There is no difference in the noise spectrum between the single pixel read out and the vertical binning. The noise spectrum with horizontal binning has again a higher photoelectron rate and a higher gain.

The noise shows dependences that are not recorded in the datasheet. With this measurements we tried to find optimal conditions for state detection with a signal to noise ratio that is as good as possible. We learned that the lowest noise can be obtained by using vertical binning and the external start trigger mode.

Since we can only bin pixels perpendicular to the dipole trap we had to ro-

tate the camera and we had to change the experimental control in order to communicate with the camera.

### stray light

Everything presented in this section so far are effects of the camera itself. An additional noise source is stray light. Photons can hit the CCD that are not emitted by atoms but by any other source.

## 4.5 Modelling the Count Distribution

The threshold method does not require any knowledge about the origin of the distribution. Nevertheless, it is important to know what the limiting effects for the state detection are. Without a functional model it is not possible identify the limiting effects. For this we developed an analytic model for the count distributions when atoms are imaged in the bright and dark state. To develop such a model one needs two things. The photon distribution  $D_{\text{ph}}(n)$  and the response of the CCD camera.

As it was found in chapter 4.4 the distribution of counts of a single photoelectron is exponentially distributed. If now multiple photons hit the CCD, multiple photoelectrons are created and amplified independently of each other. Therefore the  $n$  photoelectron distribution can be calculated by the convolution of  $n$  single photon distributions.

$$D_n(c) = \underbrace{D_1(c)D_1(c)\cdots D_1(c)}_{n \text{ times}} \quad (4.5a)$$

$$= c^{n-1} \frac{e^{-\lambda c}}{\lambda^n n!} \quad (4.5b)$$

This distribution is known as the Erlang distribution [39]. Of course, the read out noise has to be also included. Analogous to chapter 4.4 this leads to a corrected  $n$  photoelectron distribution  $D_n^{\text{corr}}(c)$

$$D_n^{\text{corr}}(c) = D_n(c) * D_{\text{read}}(c) \quad (4.6)$$

The analytical solution for formula 4.6 is given in formula A.1 in the appendix. This formula was calculated with mathematica. In principle the effect of the sCIC could also be included. This is not done since sCIC are not as likely as CIC and they produce less counts. Therefore their effect is

not severe. Additionally the consideration of sCIC would increase the computational effort to use the distribution.

While imaging photons emitted by an atom hit different pixels in the ROI and therefore more than one pixels have to be taken into account. If  $n_1$  photons hit the first pixel  $n_2$  photons hit the second pixel and so on the overall distribution of counts in ROI of  $m$  pixels is given by

$$D_{\text{ROI}}(c) = D_{\text{pixel 1}}(c) \cdots D_{\text{pixel } m} \quad (4.7a)$$

$$= D_{n_1}^{\text{corr}}(c) \cdots D_{n_m}^{\text{corr}}(c) \quad (4.7b)$$

$$= \underbrace{D_{\text{read}}(c) \cdots D_{\text{read}}(c)}_{m \text{ times}} D_{n_1}(c) \cdots D_{n_m}(c) \quad (4.7c)$$

$$= \underbrace{D_{\text{read}}(c) \cdots D_{\text{read}}(c)}_{=: D_{\text{read, ROI}}} \underbrace{D_1(c) \cdots D_1(c)}_{n = n_1 + n_2 + \dots \text{ times}} \quad (4.7d)$$

$$= D_{\text{read, ROI}} D_n(c) \quad (4.7e)$$

The term  $D_{\text{read, ROI}}(c)$  is just a  $m$  fold convolution of Gaussian with a constant width, which is a Gaussian with a width increased by a factor of  $\sqrt{m}$ . In the following the width of the read out describes the read out of a complete ROI. The term  $D_n(c)$  shows that it is sufficient to treat the the overall number of photons and that hit the CCD and it is not necessary to treat every pixel individually.

The other part which is needed to explain the distribution of counts is the photon distribution. For the dark state this is very simple. The atom does not scatter any photons. In principle the atom could be off resonantly excited in the bright state but because of the big hyperfine separation between the Rubidium ground state (see chapter 2.1) this is very improbable and can be neglected.

$$D_{\text{ph}}^{\text{D}}(n) = \delta_{0,n} \quad (4.8)$$

For the bright state this is more complicated. There are three possible ways why the atom should stop emitting photons. First, the imaging time has passed and the atom is not longer exposed to the imaging light. Second, it can be off resonantly pumped into the dark state. A third possibility is that the atom gets lost. Since we are interested in the non-destructive regime of state dependent imaging setting we choose only setting with a survival probability of above 95%. In this regime we can neglect effect of

atom loss on the bright state distribution. An analytical model of the photon distribution neglecting atom loss can be found in [35]

$$D_{\text{ph}}^{\text{B}}(n) = \frac{e^{-(1+\alpha'/\eta)\lambda_0} \lambda_0^n}{n!} + \frac{\alpha'/\eta}{(1+\alpha'/\eta)^{n+1}} \Gamma(n+1, (1+\alpha'/\eta)\lambda_0). \quad (4.9)$$

Here  $\alpha'$  is the leakage probability per emitted photon,  $\eta$  the detection efficiency and  $\lambda_0$  the mean number of detected atoms when the atom stays on the cycling transition the complete imaging time. In the following I will use the leakage probability per detected photon  $\alpha = \alpha'/\eta$  since the detection efficiency is not known exactly.

CIC and stray light can occur in the region of interest and have therefore to be included in the distribution. CIC happen with a constant rate independent of each other in a fixed space interval and are therefore Poisson distributed [41]. The mean of the distribution is given by  $mp_{\text{CIC}}$  where  $m$  is the number of pixels and  $p_{\text{CIC}}$  is the mean number of CIC per pixel.

$$D_{\text{CIC}}(n) = \frac{e^{-mp_{\text{CIC}}} (mp_{\text{CIC}})^n}{n!} \quad (4.10)$$

The photoelectron distribution is given as the convolution of the photon distribution and the CIC distribution

$$D_{\text{pe}}^{\text{B/D}}(n) = D_{\text{ph}}^{\text{B/D}}(n) P_{\text{CIC}}(n) \quad (4.11a)$$

$$= \sum_{i=1}^n D_{\text{ph}}^{\text{B/D}}(n-i) \frac{e^{-mp_{\text{CIC}}} (mp_{\text{CIC}})^i}{i!} \quad (4.11b)$$

Note that the dark state photoelectron distribution is the CIC distribution. Now the distribution of photoelectrons and the distribution of counts for arbitrary photoelectrons is known and the distribution of counts for atoms in the bright or dark state can be calculated.

$$D_{\text{B/D}}(c) = \sum_{n=0}^{\infty} D_{\text{pe}}^{\text{B/D}}(n) D_n^{\text{corr}}(c) \quad (4.12)$$

Note that here  $D_n^{\text{corr}}(c)$  contains the read out noise of the whole ROI. With formula 4.6.1 the bright state and dark state distribution can be completely described with six parameters. Those are summarized in table 4.1

$\sigma$	standard deviation of Gaussian read out noise
$1/\lambda$	mean counts per photoelectron
$p_{\text{CIC}}$	mean number of CIC per pixel
$\alpha$	leakage probability per detected photon
$\lambda_0$	mean number detected photons if the atom remains bright
$m$	number of pixels in ROI

Table 4.1: Meaning of the distribution parameters.

## 4.6 Monte-Carlo Simulation

The imaging process can also be simulated. Since the analytic model is known one could think that the simulation is not necessary because one can calculate the detection error instead of simulating it but there is a reason why a Monte Carlo Simulation is important. In chapter 5 I will use Monte Carlo simulations that include the spatial spread of the counts. There is no analytic model that gives the detection error in this case. Therefore it is important to show that the Monte Carlo simulation indeed is equivalent to the analytic treatment.

### 4.6.1 Working Principle of the Simulation

The input of the simulation are the five distribution parameters. With this parameters the distributions defined in are simulated. From this one can easily extract the detection error this is depicted in figure 4.9. The dark state and the bright state atoms are simulated independently.

**Dark state:** Only the read out noise and the CIC contribute. First the read out noise is added by generating a Gaussian distributed random number with a width of  $\sqrt{m}\sigma$ . For each atom he number of CIC is Poissionian distributed with a mean of  $mp_{\text{CIC}}$ . For each atom the number of CIC is randomly assigned following this distribution. Since there are no incident photons the number of CIC is equal the number of photoelectrons  $n$ . The camera response is inserted by adding a  $n$  random numbers from a exponential distribution (mean  $1/\lambda$ ) independently. With this the final number of counts is reached.

**Bright state:** Atomic fluorescence creates additionally incident photons. The photon distribution follows formula 4.9. The number of incident photons is added to the number of CIC and one gets the number of photoelectrons  $n$ .

The number of counts for an atom is calculated in the very same way as it is for atoms in the dark state. We still need to generate the number of incident photons.

To do so one has to simulate the photon distribution. The time atoms spend on the cyclic transition is exponentially distributed. The lifetime  $\tau$  is can be extracted from the distribution parameters. For this one needs the scattering rate  $R_{\text{sc}}$ . When an atom stays on the cyclic transition the complete imaging time  $t_{\text{D}}$  we collect in mean  $\lambda_0$  photons. Therefore

$$R_{\text{sc}} = \frac{\lambda_0}{\eta t_{\text{D}}}. \quad (4.13)$$

The mean number of photons scattered before the atom falls into the dark state is  $\alpha'^{-1}$ . The lifetime is the time which is needed to scatter that many photons. Therefore

$$\tau = \frac{1}{\alpha' R_{\text{sc}}} = \frac{t_{\text{D}}}{\lambda_0 \alpha}. \quad (4.14)$$

A bright atom the time  $t$  on the cycling transition. The time  $t$  is randomly assigned following an exponential distribution with mean  $\tau$ . In the time  $t$  the expectation value of detected photons is given by

$$\bar{N}_{\text{ph}} = \lambda_0 \frac{t}{t_{\text{D}}}. \quad (4.15)$$

Of course the atom can not scatter photons longer than the imaging time. Every  $t > t_{\text{D}}$  is therefore set to  $t = t_{\text{D}}$ . The actual incident photons is a random number from a Poisson distribution with an mean of  $\bar{N}_{\text{ph}}$ . This is done for  $N$  atoms independently.

## 4.6.2 Results of the Simulation

It is important that the simulation give the very same result as the analytic model. Figure 4.9 shows the simulated bright and dark state distribution. This results include 10 million individual simulated atoms. The distribution parameters given in 4.2.

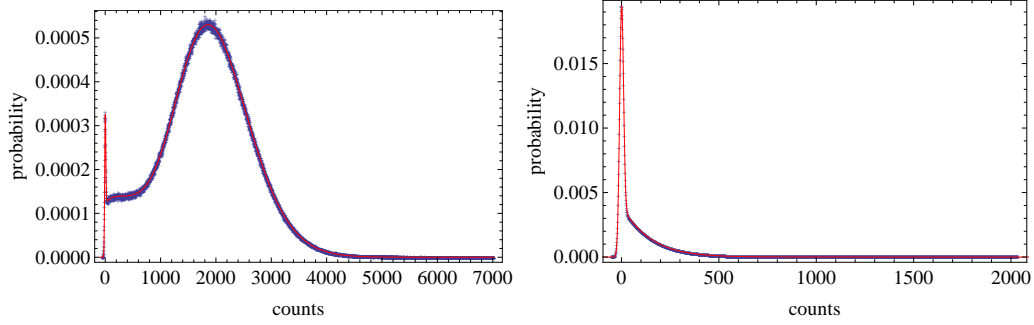


Figure 4.9: Simulated data and analytic model for the bright state (top) and the dark state (bottom). Perfect agreement between both.

$\lambda$	0.01
$\alpha$	0.015
$\lambda_0$	20
$p_{\text{CIC}}$	0.15
$\sigma$	4.5

Table 4.2: Parameters for the simulation of bright and dark state distributions

Those parameters are close to experimentally found parameters. One can see a perfect agreement between the simulated data and the analytic model. This confirms that the Monte Carlo simulation indeed works without problems.

The detection error calculated with simulated data is  $(4.295 \pm 0.006) \%$  while the analytic expressions lead to  $4.299 \%$ . Since the simulation and the analytic model lead to the same distribution the detection error is the same.

In principle the error for the detection error should be calculated with the bootstrap method. Since  $10^7$  atoms are simulated this is not possible within reasonable computational time. The shown error is the binomial error which should be similar to the one obtained with bootstrap.

From this one can tell that the results of the simulation can indeed be trusted.

## 4.7 Experimental results

In this section I will present experimental data. First I will show a starting point. Afterwards I will present a systematic search for the best possible settings. In the third part I will show that the model developed in chapter 4.5 describes experimental data very well. Afterwards I will explore the

parameter space with the analytic model. What we found in this exploration will lead to an improved state detection presented in the last part of this section.

### 4.7.1 The first try

When we tried the state detection the very first time we have had done no optimization. We did not use on chip binning. Neither the polarization of light was optimized nor the magnetic fields. No proper parameter scan was done. Nevertheless we found an detection error of

$$\epsilon = 21.3_{-3.8}^{+0.8} \% \quad (4.16)$$

The margin of error is so large because the it was a very small data set which only contained 80 atoms. Although more than a fifth of all atoms is wrongly detected this result was very promising. Without much effort we could observe a significant difference between the hyperfine states which was an encouraging result.

### 4.7.2 Frequency Scan

After this first attempt we optimized the polarization of the light to suppress off resonant excitation and used on chip binning to reduce the noise. There are three experimental parameter one can change. The trap depth, the power of the imaging light and its frequency. We started at a fixed trap depth of 3.3 mK and scanned the frequency and the power. For each frequency we took multiple data sets with different intensities. The data presented here have an survival probability of around 95 %. The detection error of every frequency is represented by the data where the survival probability is near this value.

Figure 4.10 shows the the detection error versus the frequency. The 0 in the detuning is the  $F = 2 \rightarrow F' = 3$  transition with the Stark shift due to the dipole trap included. The detection error is experimentally measured as explained in section 4.3.

One can clearly see that there is an optimal frequency to perform non-destructive state detection. This is due to two different effects. The frequency suppression of off resonant excitation is stronger the closer to resonance. Therefore atoms do not scatter many photons until they fall into the dark state if the intensity is low.

When the atom gets excited the dipole force is repulsive. Therefore the atom

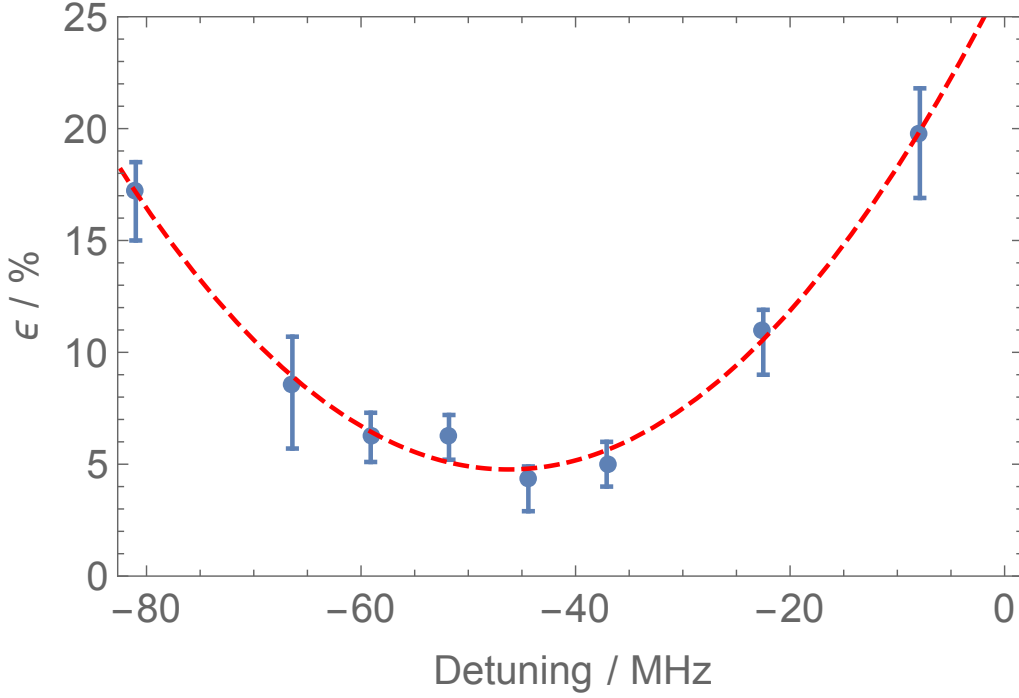


Figure 4.10: Detection error versus the frequency. Only measurements with a survival probability of around 95 % are shown. In red: fitted parabola to guide the eye

gains energy when it is in the excited state. This leads to heating [42]. By using red detuning the atom loses energy in every absorption cycle. The further the light is red detuned the lower is this atom loss.

This two effects lead to an optimal frequency of around 50 MHz red detuning. The errorbars in figure 4.10 are quite big. Every of the shown points represent a dataset of a couple of hundred measured atoms. This scan gives a reasonable estimate the detection error.

### 4.7.3 Comparison of the Model and Experimental Data

To analyse how well the analytic model developed in section 4.5 describes experimental data we did the state detection with 14'442 atoms. Using a detuning of -59.1 MHz and 1.77 saturation intensities we found a detection error of  $(8.0^{+0.1}_{-0.1})\%$  and a survival of  $(96.70 \pm 0.01)\%$ . Figure 4.11 shows the bright and the dark state distribution and the fit to the analytic model for this data set. The fit parameters are given in table 4.3.

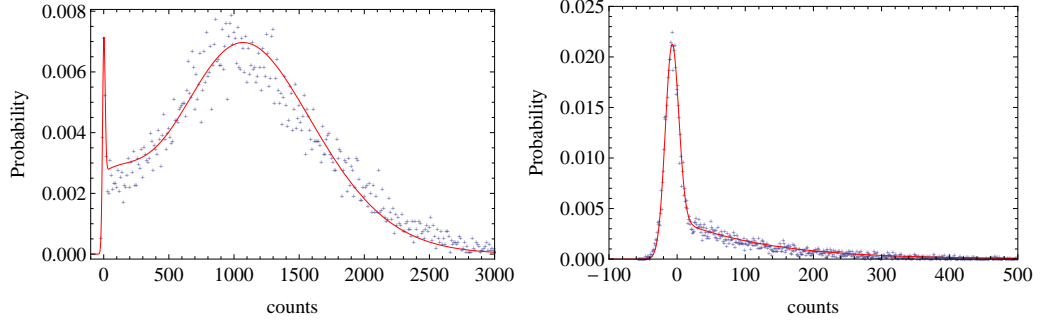


Figure 4.11: Measured bright (left) and dark state (right) histogram and the best fit (red curves)

$\lambda$	0.0111
$\alpha$	0.0302
$\lambda_0$	13.7
$p_{\text{CIC}}$	0.144
$\sigma$	4.47

Table 4.3: Fitted distribution parameters

The theoretical model explains the data quite well. One can see a couple of minor discrepancies between the data and the model. Atoms in the dark state do not scatter photons. Therefore the dark state state distribution only depend on the camera model. Since the camera model is well known it is not surprising that the model is a good fit for the data.

The bright state is effected by instabilities in the imaging conditions. Since the data was taken over several hours small changes in this conditions are not unlikely. Since the atoms are located at different positions the Stark shift is not perfectly equal for all of them. Therefore the atoms have slightly different transition frequencies due to the slightly different Stark shift. The model for the photon distribution does not include lost atoms.

The data has a dominant very broad peak centred at around 1200 counts. The data suggests a slightly broader peak than the fit. The data look somehow tilted. This could be explained by the combination of two things. The different transition frequencies and possible minor instabilities in the imaging conditions might cause a broadening while the atoms that emit many photons are more likely get lost. From those atoms we detect most photons. This would cause a asymmetry in the dominant peak which might look like a small tilt of this peak.

For very small count rates there is an additional very sharp peak. This peak is included in both, the data and the model. This peak is caused by atoms where we do not detect any photons.

From those figure 4.11 one can tell that the model developed in chapter 4.5 indeed describes the imaging process.

#### 4.7.4 Parameter Scan with Analytic Model

Since the model developed in section 4.5 does describe the experimentally found data I have performed a parameter scan. This means that I have calculated the detection error for a set of distribution parameters using the analytic distributions defined by those distributions. From this we can extract the main limitations for the detection error.

The read out noise depends of the camera and we will use maximum gain. Therefore I chose the width of the read out noise  $\sigma$  and the mean number of counts per photons  $1/\lambda$  to be constant. I did not change the mean number of photons in the Poissonian peak  $\lambda_0$ . Since the bright state distribution is dominated by leaked atoms in the threshold region a change in  $\lambda_0$  has very little influence on the detection error. Those three parameters are

$$\lambda = 0.00993, \quad \sigma = 4.624, \quad \lambda_0 = 19. \quad (4.17)$$

Figure 4.13 shows the detection error versus the  $p_{\text{CIC}}$  for various  $\alpha$ . The detection error is lowest when the leakage probability and the number of CIC is lowest which is not surprising. The slope of the detection error function is high for low values of  $p_{\text{CIC}}$  and gets smaller the higher  $p_{\text{CIC}}$  gets. The same is true for  $\alpha$ . The differences between the graphs get larger for higher  $\alpha$  although the chosen values of  $\alpha$  are equidistant.

For realistic parameters this means that a suppression of leakage can change the detection error more than a reduction of the CIC. One would have to reduce the CIC very strongly until it enters a regime were the detection error is significantly lower. Since we put much effort in finding the optimal settings of the camera I doubt that this is possible. Nevertheless, a further reduction of  $\alpha$  must still be possible.

#### 4.7.5 Optimized Magnetic Fields

In the last section it was shown that a reduction of the leakage rate would strongly reduce the detection error. We therefore optimized the polarization of the state detection light. We optimized the magnetic field such that the

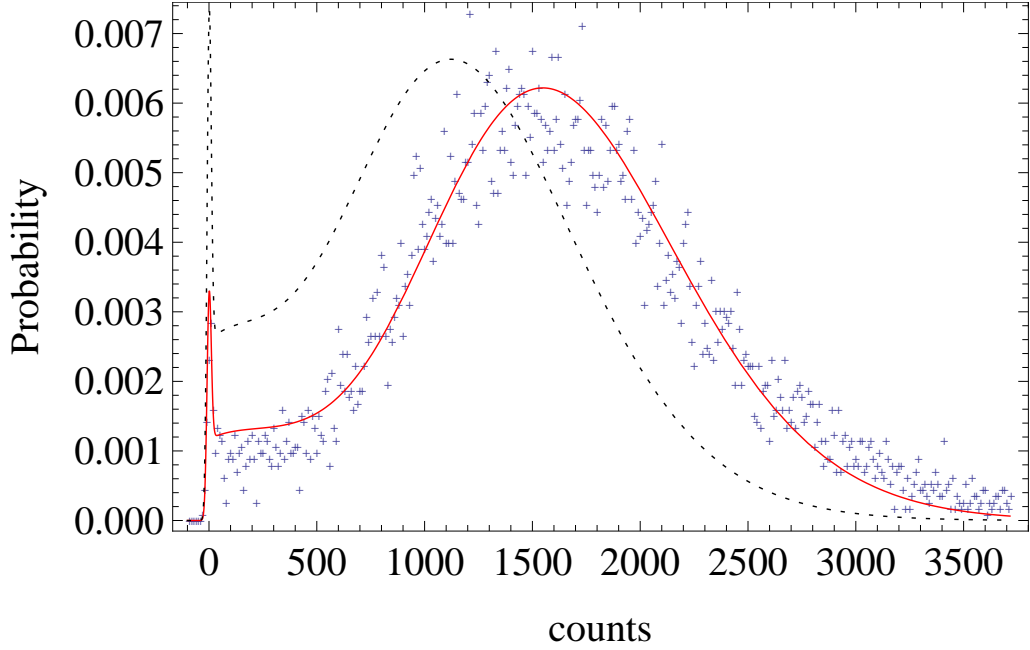


Figure 4.12: Measured probability distribution of the bright state using the optimized magnetic fields. Each point is measured by the combined occurrences of 10 neighbouring counts. The red line is the best fit to this data while the black dotted line is the best fit to the data from section 4.7.3. 11385 individual state detection measurements contributed.

quantization axis due to the magnetic field is in parallel to the propagation direction of the light.

Figure 4.12 shows the bright state distribution data taken with the optimized magnetic field including the best fit (red). The black dotted line is the fit from section 4.7.3. One can clearly see that the leakage is suppressed with the optimized fields. For this settings the fit parameter are given in table 4.4.

$\lambda$	0.0106
$\alpha$	0.0133
$\lambda_0$	17.7
$p_{\text{CIC}}$	0.138
$\sigma$	4.41

Table 4.4: Fitted distribution parameters

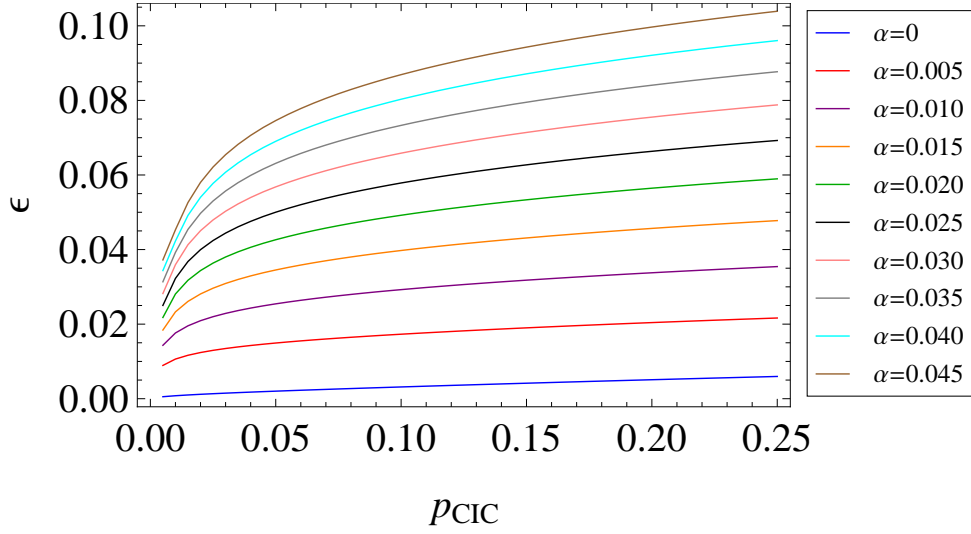


Figure 4.13: Calculated detection error versus the mean number of CIC per pixel for various leakage probabilities.

With this setting  $\alpha$  is reduced by a factor of around 2.5. This means that 2.5 times more photons can be scattered before the atoms are pumped in the dark state. The camera parameters are very similar to the ones in the parameter scan. From this we can tell that the camera performance has not changed over a couple of months.

For a survival probability of  $S = (98.1 \pm 0.1)\%$  we find a detection error of  $\epsilon = (3.59^{+0.15}_{-0.14})\%$ . It might be possible to find slightly better settings by doing a parameter search like in chapter 4.7.2 but we choose to take these settings and apply the non-destructive state detection instead for decoherence studies. Those studies can be found in [32].

This method is a huge speed up of measurements. It takes around 3 seconds to reload the dipole trap. With the traditional push out technique we can only measure the atom once. For around 5 atoms per loading this results in less than two measurements per second. The whole sequence with 100 state detection takes around a second. A survival of 95% means that an atom can be measured 20 times on average. This makes it 600 measurements per loading meaning 200 measurements per second.



# Chapter 5

## Use Spatial Information to Improve State Detection Fidelity

In chapter 4 I completely neglected the fact that the structure of the fluorescence signal is known. Stray light and CIC occur on all pixels in the ROI with a constant probability while fluorescence photons hit most likely pixels in the centre of the ROI. Therefore those pixels are more important for the state detection than the outer ones.

In this chapter I will present a way of combining the information of the individual pixels using Bayesian analysis to lower the detection error.

### 5.1 Bayesian Analysis

Bayes' theorem give a possibility to include the spacial information in a probability theoretical consistent way.

#### 5.1.1 Bayes' Theorem

There are only two formulae that together with some logical arguments build the complete foundation of probability theory. Thus are the sum rule (equation 5.1a) and the product rule (equation 5.1b) [43, 44].

$$P(X) + P(\bar{X}) = 1 \quad (5.1a)$$

$$P(X, Y) = P(X|Y)P(Y) = P(Y|X)P(X) \quad (5.1b)$$

Here  $P(X)$  is the probability that  $X$  is true,  $P(X, Y)$  the probability that  $X$  and  $Y$  are simultaneously true and  $P(X|Y)$  is the probability that  $X$  is true under the condition that  $Y$  is true (conditional probability).

From those two formulae Bayes' theorem (equation 5.2a) and the marginalization (equation 5.2b) directly follow [43, 44].

$$P(X|Y) = \frac{P(Y|X)P(X)}{P(Y)} \quad (5.2a)$$

$$P(X) = \sum_Y P(X, Y) \quad (5.2b)$$

When there are multiple possible events  $\{E\}$  Bayes' theorem can be combined with the marginalization to

$$P(X|Y) = \frac{P(Y|X)P(X)}{\sum_{E \in \{E\}} P(Y|E)P(E)} \quad (5.3)$$

The meaning of this formula becomes clear if one understands  $Y$  as a measurement and  $\{E\}$  as a set of possible explanation for this measurement. Then  $P(X|Y)$  gives the probability that explanation  $X \in \{E\}$  is true if  $Y$  is measured.

For single atom state detection there are only two possibilities. Therefore the set  $\{E\}$  only has two elements. The atom is dark  $D$  or the atom is bright  $B$ . The measurement is a single pixel count rate  $c$ . Thus equation 5.3 can be used to calculate the probability that the atom is bright

$$P(B|c) = \frac{P(c|B)P(B)}{P(c|B)P(B) + P(c|D)P(D)} \quad (5.4)$$

This probability now depend on two things. First, the probability to measure  $c$  under the condition that the atom is bright (dark)  $P(c|B)$ . This is nothing else but the single pixel bright (dark) state distribution. Second, the probability that the atom is bright (dark). Note that this is not what we want to calculate. Formula 5.4 gives the probability that the atom is bright under the condition that  $c$  is measured while  $P(B)$  does not depend on this measurement. In other words,  $P(B)$  is the probability before the measurement (a priori  $P_B^{\text{prior}}$ ) and  $P(B|c)$  the probability after the measurement (a posteriori  $P_B^{\text{post}}$ ).

We want to use Bayes' theorem to calculate the probability that the measured fluorescence pattern arose from a bright atom. Using the single pixel

distribution of counts we can apply formula 5.4 iteratively for all pixels in the region of interest.

The a posteriori probability that was found after the first pixel can deal as the a priori probability for the analysis of the second pixel and so on. Since before the first pixel is analysed there is no information about the atomic state and therefore the a priori probability of the first pixel is 0.5.

### 5.1.2 Weighting

As explained in chapter 4.3 the analysis programme computes the LSF. This LSF is the form of the single atom intensity distribution. Speaking of a single photon this means that the LSF is the spatial distribution of where the photon hits the CCD camera. Figure 5.1 shows an experimentally found LSF. The probability that a photon hits pixel  $i$  is given by

$$M(i) = \int_{d(i)-0.5}^{d(i)+0.5} dy \text{LSF}(y) \quad (5.5)$$

where  $d(i)$  is the distance of the center of pixel  $i$  to the centre of the LSF, the fitted position. Since the pixel is spatially extended one has to integrate the probability distribution over its area.

### 5.1.3 Single Pixel Count Distributions

The last thing that is needed to use Bayes' theorem for state detection are the single pixel count distributions. I developed them analogous to the overall count distribution shown in chapter 4.5.

The  $n$  photoelectron distribution is given by formula 4.6. Note that here I use the single pixel read out noise. The detection efficiency  $\eta$  is the probability that a emitted photon is detected. The weighting formula 5.5 gives the probability that a detected photon is detected in pixel  $i$ . Therefore the detection efficiency of pixel  $i$  is given by

$$\eta_i = \eta M(i) \quad (5.6)$$

For the dark state distribution this does not change anything since no photons are emitted and therefore the photoelectron distribution is the Poissonian CIC distribution with the mean  $p_{\text{CIC}}$ . In the case of bright atoms the detection efficiency of in formula 4.9 can be substituted by  $\eta_i$ . By this the

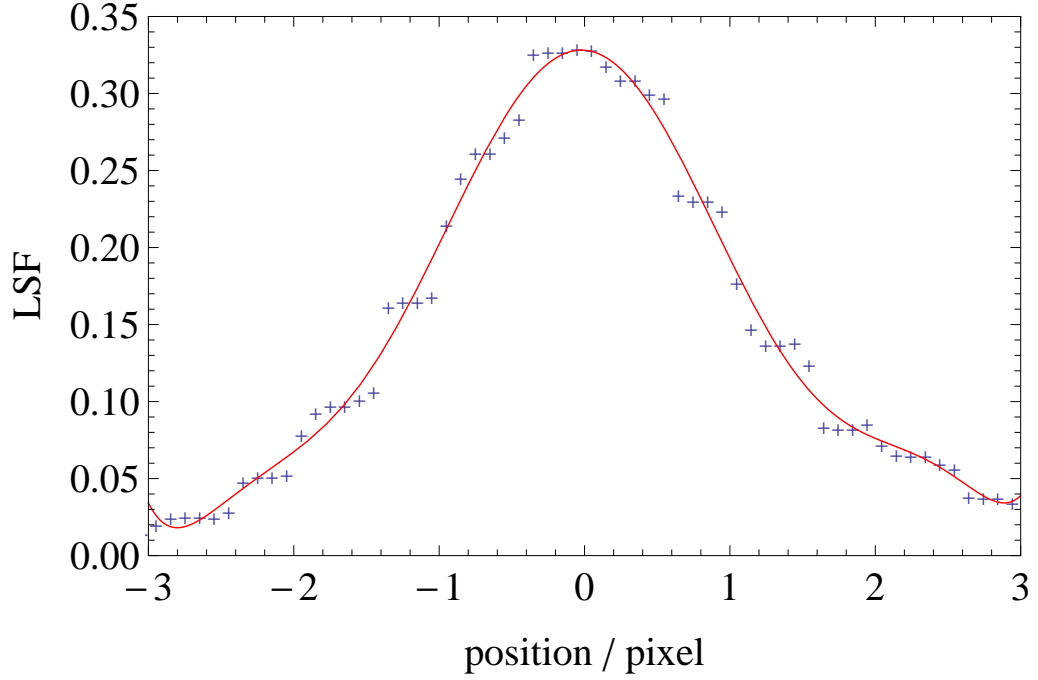


Figure 5.1: Experimentally found LSF. In red: fitted eight order polynomial for analytic treatment

single pixel photon distribution can be given as a function of the weighting factor  $M$ .

$$D_{\text{ph}}^{\text{B}}(n, M) = \frac{e^{-M\lambda_0(1+\alpha/M)} M^n \lambda_0^n}{n!} + \frac{\alpha/M}{(1 + \alpha/M)^{(n+1)}} \Gamma(n+1, M\lambda_0(1+\alpha/M)) \quad (5.7)$$

Analogous to chapter 4.5 this bright state photonelectron distribution is the convolution of the CIC distribution and the photon distribution.

The distribution of counts for the dark state and the bright state distribution is then given by formula 4.6.1, modified by the weighting factor  $M$ .

$$D_{\text{D}}(c) = \sum_{n=0}^{\infty} D_{\text{pe}}^{\text{D}}(n) D_n^{\text{corr}}(c) \quad (5.8a)$$

$$D_{\text{B}}(c, M) = \sum_{n=0}^{\infty} D_{\text{pe}}^{\text{B}}(n, M) D_n^{\text{corr}}(c) \quad (5.8b)$$

With this distributions the Bayesian 'update' formula can be defined as

$$P_B^{\text{post}} = \frac{P_B(c, M)P_B^{\text{prior}}}{P_B(c, M)P_B^{\text{prior}} + P_D(c)(1 - P_B^{\text{prior}})} \quad (5.9)$$

Note that here the fact that  $P_D = 1 - P_B$  is used. This formula can be applied iteratively for every single pixel count rate in the ROI and by this the overall probability that the atom is bright is calculated. If this probability is above 0.5 I will consider the atom as bright. The detection again the fraction of wrongly detected atoms.

## 5.2 Experimental Results

If the Bayesian method is applied to real data there are several steps to do. First, one needs to find the ideal distribution parameters. The parameters  $\sigma$ ,  $p_{\text{CIC}}$  and  $\lambda$  are found by fitting the dark state distribution while  $\lambda_0$  and  $\alpha$  are found by fitting the bright state distribution. Additional to this one needs the LSF to find an optimal weighting. This is a key feature of the image analysis toolbox can easily be extracted. With formulae 5.8b and 5.8a the single pixel bright and dark state distributions can be calculated. Using formula 5.9 the probability that the measured counts arose from a bright atom is calculated.

Threshold	Bayes
$3.59_{-0.14}^{0.15} \%$	$2.88 \pm 0.06 \%$

Table 5.1: Measured detection error with threshold method and with Bayesian for the measurement with optimized magnetic fields

Table 5.1 shows the detection error calculated with the Bayesian analysis and with the threshold method. The Bayesian analysis let the detection error drop by 20 %.

For using the Bayesian analysis is that one needs to know the distribution of counts. Therefore one needs a big data set such that one can fit the model distribution. Therefore the Bayesian analysis is not suited to make a parameter scan.

To find good parameters one cannot use the Bayesian analysis but for using the state detection for any measurement the lower detection error of the Bayesian analysis lead to more accurate measurements. When measuring the population in the  $F = 2$  state the contrast is increased by the lower detection

error. Contrast means the difference between the measured population in the extreme cases of only bright and only dark atoms. This contrast is  $1 - 2\epsilon$ . If live feedback is given due to the state of an atom it would be even more important to use the Bayesian analysis because this would lower the fraction of wrong feedback.

### 5.3 Monte Carlo Simulation

For the Bayesian analysis there is no obvious analytic treatment for the detection error. Based on the simulation explained in chapter 4.6 I wrote a Monte Carlo simulation to test the Bayesian analysis under perfect conditions. This simulation can be used investigate how much the Bayesian analysis lowers the detection error under different imaging conditions.

Here, I describe how effective the Bayesian is for the imaging conditions of section 5.2. If the experimental found reduction of the detection error is as effective as the simulation suggest this means that we understand the imaging process and know the positions of the atoms well enough to use the Bayesian analysis as effective as possible.

#### 5.3.1 Principle of the Simulation

The simulation works in the same way as the simulation explained in section 4.6 and this is that the detected photons have to be split on the pixels according to the LSF and the atoms' position. For this the experimentally found LSF is used.

The position is randomly chosen as a real number between  $\pm\frac{1}{2}$ . This is the difference between the fitted position and the central pixels' center. If the position would be any number outside this interval the central pixel would be different. I use a random number for this because in a real experiment the atoms' position will also be randomly distributed. Every photon will independent of the other randomly hit one of the pixels in the ROI where the probability that a given pixel is determined with the weighting factor defined in formula 5.5. The counts are calculated for every pixel individually.

Afterwards the detection error is calculated with Bayesian analysis and the error of the detection error is calculated with boots trapping and 100 sub-samples.

### 5.3.2 Results of the Simulation

I simulated the detection error with the parameters found in chapter 5.2 with 100'000 atoms. Table 5.2 shows the detection error for both the experimental and modelled detection error.

	Threshold	Bayes
experimental	$3.59_{-0.14}^{0.15} \%$	$2.88 \pm 0.06 \%$
simulation	$4.06 \%$	$3.23 \pm 0.04 \%$

Table 5.2: Measured and simulated detection error with threshold method and with Bayesian for the measurement with optimized magnetic fields

The simulated and the real data both give a drop in the detection error of 20%. In other words, the Bayesian analysis is as efficient using real data as the simulation suggests.

From this we can extract that our knowledge about the atoms' positions and their fluorescence characteristics is known well enough to use the Bayesian analysis in an optimally efficient way.



# Chapter 6

## State Detection with Multiple Atoms

When we load the dipole trap we cannot control where the atoms are. It is therefore possible that two or more atoms are trapped so near to each other that their fluorescence signal overlap on the CCD. This is the case when they have a distance of 3 or less lattice sites. It is also possible to have more than two atoms very near to each other.

Since we do not load the dipole trap densely it is unlikely that there are three or more atoms very near to each other. Furthermore, it is very hard to estimate the number of atoms for a high number of atoms. Especially when the atoms are only imaged 5 ms. Because of the sparse loading our experimental data was limited to single atoms and much less two atom cases. Nevertheless systems like Mott-insulators cannot resolve single atoms and state detection is restricted to the push out technique. Those experiment would very much profit from a non-destructive state detection state detection method.

### 6.1 Two Atom Case

The two atom case is the only one we realized in the experiment. We do not load the dipole trap very densely. Because of this most atoms are single atoms. Nevertheless, two atoms are loaded very near too each other happens in few per cent of loadings. In chapter 4 and 5 those cases we neglected those until one of the two atoms get lost and a single atom remains.

The distance between the atoms is not constant but can be any integer number of lattice sites. Therefore it is hard to define a ROI for the atoms. Using the Bayesian analysis it is not necessary to define a ROI for the individual

atoms. It is sufficient to define a combined ROI for the two atoms. The size of the ROI is similar two the single atom ROI two additional pixel to the right of the right atom and two additional pixels to the left of the left atom.

### 6.1.1 Bayesian Analysis

The main difference in the analysis of two atoms which are close to each other is that there are four possible combination of atoms. Either both atoms are bright (BB), both atoms are dark (DD), the left atom is bright and the left atom dark (BD) or the other way around (DB). For all those combinations the probability can be calculated with Bayes' theorem. From formula 5.3 one gets

$$P(X|c) = \frac{P(c|X)P(X)}{\sum_E P(c|E)P(E)} \quad (6.1)$$

We need to know the different distributions. Instead of one weighting parameter every pixel have two parameters  $M_{i,1}$  and  $M_{i,2}$  with respect to the first and second atom respectively. Since we do not expect any photons from dark atoms three of the four distributions are straightforward to define. With the single atom bright and dark state distributions defined in formulae 5.8a and 5.8b

$$P(c|DD) = D_D(c) \quad (6.2a)$$

$$P(c|BD) = D_B(c, M_{i,1}) \quad (6.2b)$$

$$P(c|DB) = D_B(c, M_{i,2}) \quad (6.2c)$$

In the case of two bright atoms photons of two independent sources can hit the pixel. Therefore the photon distribution is the convolution of the two single pixel photon distributions

$$D_{\text{ph}}^{\text{BB}}(n, M_{i,1}, M_{i,2}) = D_{\text{ph}}^{\text{B}}(n, M_{i,1}) * D_{\text{ph}}^{\text{B}}(n, M_{i,2}) \quad (6.3a)$$

$$= \sum_{i=0}^n D_{\text{ph}}^{\text{B}}(i, M_{i,1}) D_{\text{ph}}^{\text{B}}(n-i, M_{i,2}) \quad (6.3b)$$

From this photon distribution the distribution of counts  $P(c|BB)$  can be calculated in the very same manner as showed in section 5.1.3. With formula 6.1 the probability of all can be calculated iteratively in the same manner as explained for the single atom case. After all pixels have been analysed I choose the combination with the highest probability to be the measured atomic state.

### 6.1.2 Experimental realisation

Since we cannot address individual atoms in the dipole trap we cannot prepare the BD and DB combination but only the BB and DD state. We therefore do not have an experimental sequence especially built up for the two atom state detection but use the data of the single atom sequence where two atoms by chance are loaded near to each other.

We assume that the pumping works so well that all atoms are in the state we prepared them. The detection error is defined as the fraction of wrongly detected atoms. This is equivalent to the definition of the detection error in chapter 5.1.3 if an equal number of bright and dark atoms are investigated. In the analysis we only take those data into account where both atoms survived.

In the set of data that is analysed in the sections 4.7.5 and 5.2 there were 553 analysed two atom ROIs. A detection error of  $4.4_{-0.8}^{+0.9}$  %. The detection error is the fraction of wrongly detected atoms. Note, that since we cannot prepare the BD and DB state this error is not averaged over all combinations. The detection error is not much worse than the single atom detection error. This is because the detection error is averaged over the distance. As we will see in the following chapter the Bayesian analysis is very powerful when the atomic distance is larger than the standard deviation of the LSF. This is the case for a distance of two or more lattice sites. Therefore the detection error is still near the single atom detection error.

## 6.2 Simulated Many Atom State Detection

The method presented in 6.1 can in principle be extended to an arbitrarily large number of atoms. The number of possible combinations is given by  $2^N$  where  $N$  is the number of atoms which leads to a computationally extremely intense problem.

A simulation gives the possibility to investigate the many atom case in a controlled situation. Here I simulated a string of equally spaced atoms which is something we cannot prepare in the experiment.

### 6.2.1 Different Analysis Methods

To analyse how well suited the Bayesian analysis is for perform state detection for these strings I compared the detection error calculated with the Bayesian method with two other methods.

In all methods I calculated the detection error for a ROI containing a different

number of pixels and chose the number of pixels with the lowest detection error to represent the detection error of the given method.

### Threshold Method

The counts in the ROI are summed together. Afterwards the distribution of counts for a bright central atom and a dark central atom are determined and the optimal threshold is calculated analogous to chapter 3.

### Maximum Likelihood Method

The Maximum Likelihood (ML) method is used for the analysis of ion chains [36]. In this method the likelihood that the atom is bright is calculated under consideration of the next neighbours and compared with the likelihood that the atom is dark.

The likelihood that the atom is bright  $\rho(B)$  or dark  $\rho(D)$  can be given as [36]

$$\rho(B) = \prod_{i \in \text{ROI}} P(c_i | B, \mu, \nu) \quad (6.4a)$$

$$\rho(D) = \prod_{i \in \text{ROI}} P(c_i | D, \mu, \nu) \quad (6.4b)$$

where  $P(c_i | B, \mu, \nu)$  is the probability that the count  $c_i$  is measured under the condition that the atom is bright and its neighbouring atoms are in the state  $\mu$  and  $\nu$  respectively. Similar to the Bayesian analysis one has to include the model for the analysis to get the probability functions. There are four possible sources for photons. Those are the background and the three atoms. Therefore

$$P(c_i | B, \mu, \nu) = P_{\text{Pois}}(c_i, r_{\text{BG}}) \otimes P_{\text{Pois}}(c_i, M_{i,j-1} r_{\text{ph}}) \otimes P_{\text{Pois}}(c_i, M_{i,j} r_{\text{ph}}) \otimes P_{\text{Pois}}(c_i, M_{i,j+1} r_{\text{ph}}) \quad (6.5a)$$

$$= P_{\text{Pois}}(c_i, r_{\text{BG}} + (M_{i,j-1} + M_{i,j} + M_{i,j+1}) r_{\text{ph}}) \quad (6.5b)$$

The biggest conceptual difference of this method to all others I present is that one needs an initial guess (e.g. all atoms are dark). In a first step of the analysis process the likelihood to be bright or dark is calculated for all atoms. The states of its neighbours is given by the initial guess. This is done with all atoms. The atoms of which the likelihood to be bright is higher than the one to be dark are considered bright afterwards. This 'updated' states of individual atoms functions as an initial guess for the second iteration. This

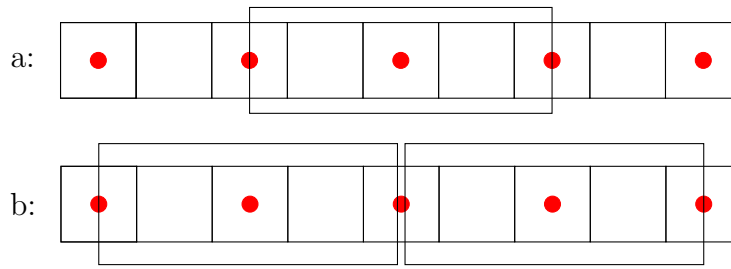


Figure 6.1: 5 atoms (red dots) imaged on a array of array of pixels. In a: ROI of the central atom. In b: ROI of the two atoms next to the central one

sequence is repeated until one iteration does not change the state of any atom.

Another conceptual difference to the other methods is that it is not possible to detect the state of a single atom. One always has to detect the state of the complete atomic ensemble.

### Bayesian Analysis

As already mentioned a Bayesian analysis which contains all atoms is not desirable since the effort of performing the state detection scales exponentially with the number of atoms. In this 5 atom scenario there would only be 32 possibilities which would be realizable but we are interested in a method for arbitrarily large atomic numbers. Therefore I will do the same approximation as for the ML method. Only the next neighbours influence the counts inside the ROI of an atom.

In a ROI of an atom one can calculate the probability for all eight possible combinations. One can show (A.2.1) that Bayes' theorem gives the same probability functions as the maximum likelihood method uses. With this functions one can calculate the probability for all eight possible combinations in a ROI. The probability that an atom is bright is then given as the sum of the probabilities of all those combinations that assume the atom to be bright.

As one can see in figure 6.1 an atom does not only contribute to the counts inside its own ROI but also in the ones of its neighbours. Therefore the probability that the atom is bright can also be calculated in the neighbouring ROI. Bayes' theorem enables us to combine this probabilities in an update scheme similar to the one presented in chapter 5.1. Again the starting probability that the atom is bright is 0.5 since we have no background information. With

the probabilities one finds in all three ROI one can update the probability according to

$$P_B^{\text{post}} = \frac{P_B(i)P_B^{\text{prior}}}{P_B(i)P_B^{\text{prior}} + (1 - P_B(i))(1 - P_B^{\text{prior}})} \quad (6.6)$$

where  $P_B(i)$  denotes the probability that the atom is bright which can be found in ROI  $i$ . The proof that one can combine the information in this manner can be found in appendix A.2.2. After this is done for all ROI all atom where the final  $P_B$  is greater than 0.5 are considered bright.

### 6.2.2 The Simulation

In a toy model I simulated the state dependent imaging of a chain of 5 equally spaced atoms. I calculated the detection error with the three different methods. In the case of the maximum likelihood method I additionally compared the extreme cases of initial guess. I assumed the atoms would be either all bright or all dark.

In each trial every atom was randomly set to be either dark or bright independently. To lower the computational effort for the state detection the count statistics were simplified. There is a dark count rate which forms a background. I modelled this by assigning a random number that follows a Poisson statistics with the mean of the dark count  $r_{\text{BG}} = 0.2$ . This is about the number of photoelectrons I found by fitting the dark state distribution to actual data in section 4.7.5. For the same reason I assumed the bright atoms to emit in mean  $r_{\text{ph}} = 20$  photons onto the detector. The number of detected photons is also Poissonian distributed

Analogous to section 4.6 I divided those photons onto the individual pixels according to the LSF. The LSF I assumed to be Gaussian with a standard deviation of  $\sigma_{\text{LSF}}$ . Since the photons of all atoms have to get divided one gets a set of weighting parameters  $M_{i,j}$  where  $i$  denotes the pixel and  $j$  the atom. The number of photons a bright atom at position  $j$  causes on the pixel  $i$  is a Poissonian distributed with a mean of  $M_{i,j}r_{\text{ph}}$ . Dark atoms do not emit any photons. Therefore  $M_{i,j} = 0$  if the atom  $j$  is dark.

For a fixed atomic distance  $a$  the I varied the standard deviation of the LSF and calculated the detection error as a function of the resolution  $R$ .

$$R = \frac{\sigma_{\text{LSF}}}{a} \quad (6.7)$$

Note that I only calculated the detection error of the central atom since this is the atom where the cross-talk effects are most severe.

### 6.2.3 Simulation Results

I analysed two different sets of measurements. In the first one I choose an atomic spacing between  $a = 10$  pixels and in the second one I choose it to be  $a = 20$  pixels. Figure 6.2 shows the detection error versus the resolution  $R$ . The lower the resolution the better individual atoms can be detected.

The better the resolution the better is the detection error with all methods. This is not surprising since for good resolution the two fluorescence signals are well separated and therefore crosstalk is less severe. Cross-talk is the main detection limitation.

For resolutions higher than 1 the threshold method outperforms the other methods. This is because the assumption that there is only cross talk between next neighbours fails for very bad resolutions. Therefore we put a wrong models into the calculation of the likelihood functions. The threshold method does not need any model input.

The Bayesian method outperforms the Maximum Likelihood method. This can also be explained by wrong assumptions. In the Maximum Likelihood method one assumes that the state of the neighbouring atoms are known. If the detection error is high it is quite probable that the states which are assumed for the neighbouring atoms is wrong. The Bayesian method does not assume that the neighbouring states are known. Therefore wrongly detected neighbouring atoms cannot have any effect.

One can additionally see that the Maximum Likelihood method gives better results for bad resolutions if the atoms are assumed to be dark in the beginning. It seems like it is worse assuming crosstalk of a neighbouring atom when there is no than assuming no crosstalk when there is.

For bad resolution there is no difference between the detection error for the data sets with an atomic spacing of 10 pixels and those with a spacing of 20 pixels. The noise is increased by using more pixels but the cross talk is the dominant error source and therefore the detection error does not change significantly. Surprisingly, this is not true for the Maximum Likelihood method with the starting condition that all atoms are bright and  $R = 1$ .

For good resolutions the detection error is lower for an atomic distance of 10 pixels. The limit of good resolution in this context depend on the method. Using the threshold method and the Bayesian analysis this limit seems to be at around  $R = 1$ . For the Maximum Likelihood method this limit is lower.

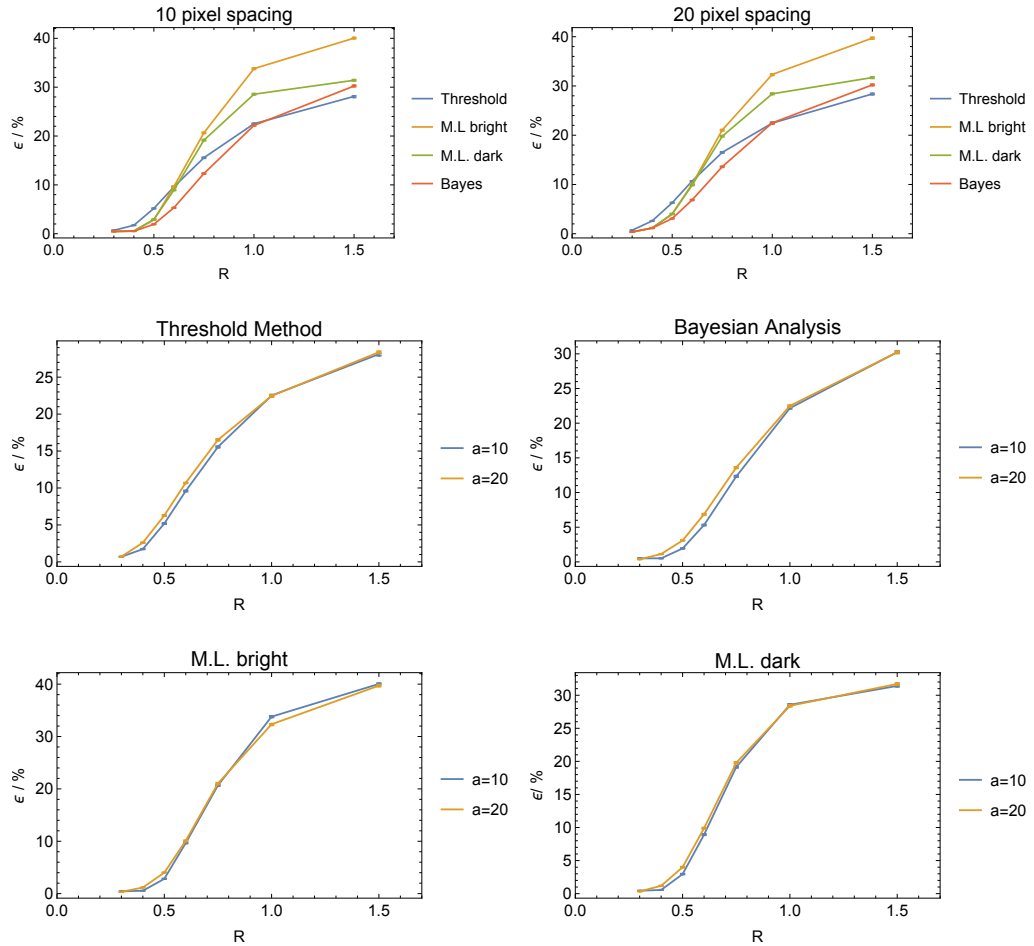


Figure 6.2: Simulated multi atom detection error versus the resolution for an atomic spacing of 10 and 20 for all four analysis methods. Top: The comparison of all analysis methods for a  $a = 10$  pixels (left) and  $a = 20$  pixels (right). Underneath: The comparison of the of the atomic distances for the threshold method (middle left), the Bayesian analysis (middle right) as well as the Maximum Likelihood method with starting condition all atoms bright (bottom left) and dark (bottom right). In all plots the statistical error are given but are too small to be seen.

# Chapter 7

## Conclusion and Outlook

This thesis can be divided in two different parts. In the first part the I described a scheme how to compress an atomic ensemble in a standing wave dipole trap. For our experimental parameters we find that around 40 % of the loaded atoms could be positioned within 10 lattice sites of the centre of the trap. The measurements agrees with a simulation and a calculation in harmonic approximation.

For Raman cooled atoms the theory overestimates the experimentally achievable compression which could be explained by a breakdown of the classical calculation close to the motional ground state.

In the future further improvements could be achieved by implementing quantum optimal control ramps for the compression sequence. Experimentally the recently upgraded the laser power for the dipole trap could also be used to further enhance the compression sequence. Furthermore, additional optical potentials could be applied for a better compression efficiency.

The second part of my thesis is concerned with the realization of simultaneous non-destructive state detection of neutral atoms in the optical dipole trap. A detailed theoretical model of the imaging process, including the imperfections of an emCCD camera, is developed and applied to optimize the state detection.

At an atom survival of 98 % we achieve a state detection error of 3.6 % for individually resolved atoms. By using Bayesian strategies to for the optimal usage of the spatial information the state detection error was further lowered to 2.9 %.

Bayesian analysis was further applied for the state detection of groups of atoms that cannot be faithfully resolved. Finally, possible strategies for the treatment of arbitrarily large atomic samples with significantly overlapping fluorescence signals have been explored.

Future work could investigate the computational performance of the various

algorithms implemented in this work. Timing performance will be crucial in order to apply the state detection in realtime for feedback purposes.

In the future we want to use Raman cooling to also improve the state detection. The main reason for losses is that the atoms are heated out of the trap due to a momentum kick by the repulsive dipole trap for an excited atom. We think that this momentum kick is smaller the colder the atoms are. Therefore Raman cooling should lead to less heating which lead to more scattered photons.

Furthermore, in the near future the fibre based cavity will be implemented in the setup leading to a whole new set of application for this experiment.

# Appendix A

## A.1 Formulae and Calculations

### A.1.1 Formulae

#### Distribution of counts for $n$ photons

The complete  $n$  photoelectron count distribution is given by

$$D_n^{\text{comp}}(c) = \frac{2^{(n-4)/2}}{(n+1)!\sqrt{\pi}\sigma} \exp\left(-\frac{c^2}{2\sigma}\right) \left[ \sqrt{2} \Gamma\left(\frac{n}{2}\right) {}_1F_1\left(\frac{n}{2}, \frac{1}{2}, \frac{(c-\lambda\sigma^2)^2}{2\sigma^2}\right) + \frac{2}{\sigma}(c-\lambda\sigma^2) \Gamma\left(\frac{n+1}{2}\right) {}_1F_1\left(\frac{n+1}{2}, \frac{3}{2}, \frac{(c-\lambda\sigma^2)^2}{2\sigma^2}\right) \right] \quad (\text{A.1})$$

where  $\Gamma(x)$  is the gamma function and  ${}_1F_1(a, b, x)$  is Kummer's function of the first kind.

### A.1.2 Calculations

#### Taylor expansion of the running wave potential

$$\begin{aligned}
U(\vec{x}) &= -T_{\text{rw}} \frac{1}{\left(1 + \frac{z^2}{z_R^2}\right)^2} \exp\left(-\frac{2r^2}{w(z)^2}\right), \text{ with } r = \sqrt{x^2 + y^2} \\
&\approx U(\vec{x})|_{\vec{x}=0} + \vec{x}^T \nabla U|_{\vec{x}=0} + \frac{1}{2} \vec{x}^T H(U)|_{\vec{x}=0} \vec{x} \\
&= -T_{\text{rw}} + \frac{1}{2} \vec{x}^T \begin{pmatrix} \frac{\partial^2 U}{\partial x^2}|_{\vec{x}=0} & \frac{\partial^2 U}{\partial_x \partial_y}|_{\vec{x}=0} & \frac{\partial^2 U}{\partial_x \partial_z}|_{\vec{x}=0} \\ \frac{\partial^2 U}{\partial_y \partial_x}|_{\vec{x}=0} & \frac{\partial^2 U}{\partial_y^2}|_{\vec{x}=0} & \frac{\partial^2 U}{\partial_y \partial_z}|_{\vec{x}=0} \\ \frac{\partial^2 U}{\partial_z \partial_x}|_{\vec{x}=0} & \frac{\partial^2 U}{\partial_z \partial_y}|_{\vec{x}=0} & \frac{\partial^2 U}{\partial_z^2}|_{\vec{x}=0} \end{pmatrix} \vec{x} \\
&= -T_{\text{rw}} \left( 1 + \frac{1}{2} \vec{x}^T \begin{pmatrix} \frac{4}{w_0^2} & 0 & 0 \\ 0 & \frac{4}{w_0^2} & 0 \\ 0 & 0 & \frac{2}{z_R^2} \end{pmatrix} \vec{x} \right) \\
&= T_{\text{rw}} \left( \frac{z^2}{z_R^2} + \frac{2\rho^2}{w_0^2} - 1 \right) \tag{A.2}
\end{aligned}$$

#### Compression rate

$$\begin{aligned}
(\sigma_x(t))^2 &= \int_{-\infty}^{\infty} dx_0 \int_{-\infty}^{\infty} dv_0 \frac{x(t)^2}{2\pi\sigma_x\sigma_v} \exp\left(-\frac{x_0^2}{2\sigma_x^2}\right) \exp\left(-\frac{v_0^2}{2\sigma_v^2}\right) \\
&= \int_{-\infty}^{\infty} dx_0 \int_{-\infty}^{\infty} dv_0 \left[ \frac{1}{2\pi\sigma_x\sigma_v} \exp\left(-\frac{x_0^2}{2\sigma_x^2}\right) \exp\left(-\frac{v_0^2}{2\sigma_v^2}\right) \right. \\
&\quad \times \left. \left( x_0^2 \cos^2 \omega t + \frac{v_0^2}{\omega^2} \sin^2 \omega t + \frac{x_0 v_0}{\omega} \sin \omega t \cos \omega t \right) \right] \\
&= \frac{1}{\sqrt{2\pi}\sigma_v} \underbrace{\int_{-\infty}^{\infty} dx_0 x_0^2 \cos^2 \omega t \exp\left(-\frac{x_0^2}{2\sigma_x^2}\right)}_{\cos^2(\omega t) \sigma_x^2} \\
&\quad + \frac{1}{\sqrt{2\pi}\sigma_v} \underbrace{\int_{-\infty}^{\infty} dv_0 \frac{v_0^2}{\omega^2} \sin^2 \omega t \exp\left(-\frac{v_0^2}{2\sigma_v^2}\right)}_{\sin^2(\omega t) \frac{\sigma_v^2}{\omega^2}} \\
&\quad + \underbrace{\frac{1}{2\pi\sigma_v\sigma_x} \int_{-\infty}^{\infty} dx_0 \int_{-\infty}^{\infty} dv_0 \frac{x_0 v_0}{\omega} \sin \omega t \cos \omega t \exp\left(-\frac{x_0^2}{2\sigma_x^2}\right) \exp\left(-\frac{v_0^2}{2\sigma_v^2}\right)}_0 \\
&= \cos^2(\omega t) \sigma_x^2 + \sin^2(\omega t) \frac{\sigma_v^2}{\omega^2}. \tag{A.3}
\end{aligned}$$

## A.2 Proofs

### A.2.1 Proof that Bayes' theorem lead to likelihood functions

The likelihood that an atom is in state  $X$  under the condition that its neighbours are in state  $\mu, \nu$  respectively is given by:

$$\rho(X) = \prod_{i \in \text{ROI}} P(c_i | X, \mu, \nu) \quad (\text{A.4})$$

I will proof that Bayes' theorem gives this besides of a normalization parameter with no initial knowledge using induction. The set of states  $(\mu, x, \nu)$  I will call  $\chi$  for simplicity

*Proof.* Let  $\Omega$  be the set of all possible combinations of bright and dark atoms  
*Base step:* The first update gives

$$P_\chi^{(1)} = P(\chi | c_1) = \frac{P(c_1 | \chi) P(\chi)}{\sum_{Y \in \Omega} P(c_1 | Y) P(Y)} \quad (\text{A.5a})$$

$$= \frac{P(c_1 | \chi)}{\sum_{Y \in \Omega} P(c_1 | Y)} \quad (\text{A.5b})$$

In the last step I used that no knowledge means that all combinations are equally probable before the Bayesian analysis starts. Since the denominator is the same for all possible combinations this is the normalisation parameter. This is exactly what formula A.4 gives for a ROI containing a single pixel.

*Inductive hypothesis:* Suppose this statement is true for all number of pixels in a ROI up to some  $k \geq 1$ .

*Induction step:* The update number  $k+1$  then gives

$$P_\chi^{(k+1)} = P(\chi | c_1, \dots, c_{k+1}) = \frac{P(c_{k+1} | \chi) P(\chi)}{\sum_{Y \in \Omega} P(c_{k+1} | Y) P(Y)} \quad (\text{A.6a})$$

$$= \frac{P(c_{k+1} | \chi) P(\chi | c_1, \dots, c_k)}{\sum_{Y \in \Omega} P(c_{k+1} | Y) P(Y | c_1, \dots, c_k)} \quad (\text{A.6b})$$

$$= \frac{P(c_{k+1} | \chi) N \prod_{i=1}^k P(c_i | \chi)}{\sum_{Y \in \Omega} P(c_{k+1} | Y) N \prod_{i=1}^k P(c_i | \chi)} \quad (\text{A.6c})$$

$$= \frac{\prod_{i=1}^{k+1} P(c_i | \chi)}{\sum_{Y \in \Omega} \prod_{i=1}^{k+1} P(c_i | \chi)} \quad (\text{A.6d})$$

which is besides of denominator that, again is the normalisation parameter formula A.4

□

## A.2.2 Proof that the update rule holds

I will proof that the update rule presented in chapter 6.2.1 holds. Let  $\Omega_1$  be the set of all possible combinations of dark and bright atoms and  $\Omega'_1 = \{Y \in Y_2 | \text{atom } i \text{ is bright}\}$  the combination in the first ROI that treat the  $i$ -th atom to be bright. Analogous  $\Omega_2$  and  $\Omega'_2$  are defined in the second ROI. Let additionally be  $\alpha = (\alpha_1, \dots, \alpha_N)$  the counts in all  $N$  pixels of the first ROI and  $\beta = (\beta_1, \dots, \beta_N)$  the counts in the second ROI.

*Proof.* The probability for a combination  $X \in Y_1$  is given by:

$$P_X(\alpha) = P(X|\alpha) = \frac{\prod_{i=1}^{k+1} P(\alpha_i|X)}{\sum_{Y \in \Omega_1} \prod_{i=1}^{k+1} P(\alpha_i|Y)} \quad (\text{A.7})$$

Since there are as many combination that consider the atom bright as there are combinations that consider it dark there is no initial bias to be either dark or bright and we can write:

$$P_B(\alpha) = \sum_{Y \in \Omega'_1} P_Y(\alpha) \quad (\text{A.8})$$

In the second ROI we do not need to begin with no initial knowledge since we have already analysed the first ROI. Instead of equal initial probabilities for all I set the initial probability to  $P_B(\alpha)/4$  for all combinations in  $\Omega'_2$  and  $P_D(\alpha)/4$  for all combinations which are not in  $\Omega'_2$ . The factor of 4 combina-

tion that treat the  $i$ -th atom as a bright one. Therefore the probability that the atom is bright can be calculated via

$$P_B(\alpha, \beta) = \sum_{Y \in \Omega'_2} \frac{P(\beta|Y)P(Y)}{\sum_{X \in \Omega_2} P(\beta|X)P(X)} \quad (\text{A.9a})$$

$$= \frac{\sum_{Y \in \Omega'_2} P(\beta|Y)P_B(\alpha)}{\sum_{X \in \Omega'_2} P(\beta|X)P_B(\alpha) + \sum_{X \notin \Omega'_2} P(\beta|X)P_D(\alpha)} \quad (\text{A.9b})$$

$$= \frac{P_B(\alpha) \sum_{Y \in \Omega'_2} P(\beta|Y)}{P_B(\alpha) \sum_{X \in Y'_2} P(\beta|X) + P_D(\alpha) \sum_{X \notin \Omega'_2} P(\beta|X)} \quad (\text{A.9c})$$

$$= \frac{P_B(\alpha)P_B(\beta)}{P_B(\alpha)P_B(\beta) + P_D(\alpha)P_D(\beta)} \quad (\text{A.9d})$$

$$= \frac{P_B(\alpha)P_B(\beta)}{P_B(\alpha)P_B(\beta) + (1 - P_B(\alpha))(1 - P_B(\beta))} \quad (\text{A.9e})$$

which can be rewritten in terms of a priori and a posteriori probabilities as

$$P_B^{\text{post}} = \frac{P_B(i)P_B^{\text{prior}}}{P_B(i)P_B^{\text{prior}} + (1 - P_B(i))(1 - P_B^{\text{prior}})} \quad (\text{A.10})$$

which is exactly formula 6.6 in the case of  $i = 2$ . That this formula holds for higher values of  $i$  can be shown by induction. This is trivial since only  $P_B(\alpha)$  has to be substituted with any initial  $P_B$ .

□



# Bibliography

- [1] W. K. Wootters and W. H. Zurek, “A single quantum cannot be cloned,” *Nature*, vol. 299, no. 5886, pp. 802–803, 1982.
- [2] C. H. Bennett, G. Brassard, C. Crépeau, R. Jozsa, A. Peres, and W. K. Wootters, “Teleporting an unknown quantum state via dual classical and einstein-podolsky-rosen channels,” *Phys. Rev. Lett.*, vol. 70, no. 13, pp. 1895–1899, 1993.
- [3] L.-M. Duan, M. D. Lukin, J. I. Cirac, and P. Zoller, “Long-distance quantum communication with atomic ensembles and linear optics,” *Nature*, vol. 414, no. 6862, pp. 413–418, 2001. [Online]. Available: <http://dx.doi.org/10.1038/35106500>
- [4] H.-J. Briegel, W. Dür, J. I. Cirac, and P. Zoller, “Quantum repeaters: The role of imperfect local operations in quantum communication,” *Phys. Rev. Lett.*, vol. 81, pp. 5932–5935, 1998.
- [5] R. Dicke, “Coherence in spontaneous radiation processes,” *Physical Review*, vol. 93, no. 1, pp. 99–110, 1954.
- [6] M. Purcell and R. V. Pound, “Proceedings of the american physical society,” *Phys. Rev.*, vol. 69, pp. 674–674, 1946.
- [7] F. Bussi eres, C. Clausen, A. Tiranov, B. Korzh, V. B. Verma, S. W. Nam, F. Marsili, A. Ferrier, P. Goldner, H. Herrmann, C. Silberhorn, W. Sohler, M. Afzelius, and N. Gisin, “Quantum teleportation from a telecom-wavelength photon to a solid-state quantum memory,” *Nature Photonics*, vol. 8, no. 10, pp. 775–778, 2014.
- [8] N. Timoney, I. Usmani, P. Jobez, M. Afzelius, and N. Gisin, “Single-photon-level optical storage in a solid-state spin-wave memory,” *Physical Review A*, vol. 88, no. 2, 2013.

- [9] X.-H. Bao, A. Reingruber, P. Dietrich, J. Rui, A. Dück, T. Strassel, L. Li, N.-L. Liu, B. Zhao, and J.-W. Pan, “Efficient and long-lived quantum memory with cold atoms inside a ring cavity,” *Nature Physics*, vol. 8, no. 7, pp. 517–521, 2012.
- [10] B. Zhao, Y.-A. Chen, X.-H. Bao, T. Strassel, C.-S. Chuu, X.-M. Jin, J. Schmiedmayer, Z.-S. Yuan, S. Chen, and J.-W. Pan, “A millisecond quantum memory for scalable quantum networks,” *Nature Physics*, vol. 5, no. 2, pp. 95–99, dec 2008.
- [11] X. Maître, E. Hagley, G. Nogues, C. Wunderlich, P. Goy, M. Brune, J. M. Raimond, and S. Haroche, “Quantum memory with a single photon in a cavity,” *Phys. Rev. Lett.*, vol. 79, no. 4, pp. 769–772, 1997.
- [12] R. Gehr, J. Volz, G. Dubois, T. Steinmetz, Y. Colombe, B. L. Lev, R. Long, J. Estève, and J. Reichel, “Cavity-based single atom preparation and high-fidelity hyperfine state readout,” *Phys. Rev. Lett.*, vol. 104, p. 203602, 2010. [Online]. Available: <http://link.aps.org/doi/10.1103/PhysRevLett.104.203602>
- [13] D. Hunger, T. Steinmetz, Y. Colombe, C. Deutsch, T. W. Hnsch, and J. Reichel, “A fiber fabry-perot cavity with high finesse,” *New Journal of Physics*, vol. 12, no. 6, p. 065038, 2010.
- [14] M. Napolitano, M. Koschorreck, B. Dubost, N. Behbood, R. J. Sewell, and M. W. Mitchell, “Interaction-based quantum metrology showing scaling beyond the heisenberg limit,” *Nature*, vol. 471, no. 7339, pp. 486–489, 2011.
- [15] M. Karski, L. Forster, J.-M. Choi, A. Steffen, W. Alt, D. Meschede, and A. Widera, “Quantum walk in position space with single optically trapped atoms,” *Science*, vol. 325, no. 5937, pp. 174–177, 2009.
- [16] J. J. Garca-Ripoll, P. Zoller, and J. I. Cirac, “Quantum information processing with cold atoms and trapped ions,” *Journal of Physics B: Atomic, Molecular and Optical Physics*, vol. 38, no. 9, p. S567, 2005.
- [17] D. Meschede and A. Rauschenbeutel, “Manipulating single atoms,” *Adv. At. Mol. Opt. Phys.*, vol. 53, p. 75, 2006.
- [18] A. Fuhrmanek, R. Bourgain, Y. R. P. Sortais, and A. Browaeys, “Free-space lossless state detection of a single trapped atom,” *Phys. Rev. Lett.*, vol. 106, p. 133003, 2011.

- [19] M. J. Gibbons, C. D. Hamley, C.-Y. Shih, and M. S. Chapman, “Non-destructive fluorescent state detection of single neutral atom qubits,” 2010.
- [20] D. A. Steck, “Rubidium 87 d line data,” Version 2.1.4, last revised 23 December 2010.
- [21] E. L. Raab, M. Prentiss, A. Cable, S. Chu, and D. E. Pritchard, “Trapping of neutral sodium atoms with radiation pressure,” *Phys. Rev. Lett.*, vol. 59, pp. 2631–2634, 1987.
- [22] M. Vangeleyn, P. F. Griffin, E. Riis, and A. S. Arnold, “Single-laser, one beam, tetrahedral magneto-optical trap,” *Opt. Express*, vol. 17, no. 16, pp. 13 601–13 608, 2009.
- [23] T. Hänsch and A. Schawlow, “Cooling of gases by laser radiation,” *Optics Communications*, vol. 13, no. 1, pp. 68 – 69, 1975.
- [24] W. Alt, “Optical control of single neutral atoms,” Ph.D. dissertation, Universität Bonn, 2004.
- [25] M. Karski, “State-selective transport of single neutral atoms,” Ph.D. dissertation, Universität Bonn, 2010.
- [26] *System Performance Andor iXon 3*, 2011.
- [27] M. T. DePue, C. McCormick, S. L. Winoto, S. Oliver, and D. S. Weiss, “Unity occupation of sites in a 3d optical lattice,” *Phys. Rev. Lett.*, vol. 82, pp. 2262–2265, 1999.
- [28] W. Alt, D. Schrader, S. Kuhr, M. Müller, V. Gomer, and D. Meschede, “Single atoms in a standing-wave dipole trap,” *Phys. Rev. A*, vol. 67, p. 033403, 2003.
- [29] R. Grimm, M. Weidemüller, and Y. B. Ovchinnikov, “Optical dipole traps for neutral atoms,” ser. *Advances In Atomic, Molecular, and Optical Physics*, B. Bederson and H. Walther, Eds. Academic Press, 2000, vol. 42, pp. 95 – 170.
- [30] T. Fließbach, *Statistische Physik - Lehrbuch zur Theoretischen Physik IV*, 5th ed. Heidelberg: Spektrum Akademischer Verlag, 2010.
- [31] P. F. Thad Walker, “Measurements of collisions between laser-cooled atoms,” *Adv. At., Mol., Opt. Phys.*, vol. 34, pp. 125–170, 1994.

- [32] L. Paulet, “Raman and microwave manipulation of a dense atomic ensemble,” Master’s thesis, Bonn, 2014.
- [33] M. Paterno, “Calculating efficiencies and their uncertainties,” 2004.
- [34] S. Kuhr, W. Alt, D. Schrader, I. Dotsenko, Y. Miroshnychenko, A. Rauschenbeutel, and D. Meschede, “Analysis of dephasing mechanisms in a standing-wave dipole trap,” *Phys. Rev. A*, vol. 72, p. 023406, 2005.
- [35] M. Acton, K. A. Brickman, P. C. Haljan, P. J. Lee, L. Deslauriers, and C. Monroe, “Near-perfect simultaneous measurement of a qubit register,” 2005.
- [36] A. Burrell, “High fidelity readout of trapped ion qubits,” Ph.D. dissertation, University of Oxford, 2010.
- [37] L. Ratschbacher, “Investigation of an atom-ion quantum hybrid system,” Ph.D. dissertation, University of Cambridge, 2013.
- [38] *Hardware Guide, Andor iXon 3*, 2011.
- [39] K. B. W. Harpsøe, M. I. Andersen, and P. Kjørgaard, “Bayesian photon counting with electron-multiplying charge coupled devices (EMCCDs),” *Astronomy & Astrophysics*, vol. 537, p. A50, 2012.
- [40] A. G. Basden and C. A. Haniff, “Low light level CCDs and visibility parameter estimation,” *Monthly Notices of the Royal Astronomical Society*, vol. 347, no. 4, pp. 1187–1197, 2004.
- [41] F. A. Haight, *Handbook of the Poisson Distribution* -. New York: John Wiley & Sons Canada, Limited, 1967.
- [42] T. A. Savard, K. M. O’Hara, and J. E. Thomas, “Laser-noise-induced heating in far-off resonance optical traps,” *Phys. Rev. A*, vol. 56, pp. R1095–R1098, 1997.
- [43] E. T. Jaynes and G. L. Bretthorst, *Probability Theory - The Logic of Science*. Cambridge: Cambridge University Press, 2003.
- [44] D. Sivia, J. Skilling, and D. S. Sivia, *Data analysis - a Bayesian tutorial*, 2nd ed. New York: Oxford University Press, 2006.

# Acknowledgements

I want to thank Professor Meschede for the opportunity to work in his group and with this very interesting experiment. Despite his very full schedule he always found time to answer all kinds of questions and helped with his experience in the scientific community.

I also thank Professor Linden for being the second corrector for my thesis. After he has supervised my Bachelor thesis he is now also a part of my second step into science.

Without the guidance of Lothar Ratschbacher and Miguel Martinez Dorantes this work would not have been possible. Miguel had so much patience explaining me how important patience is while working in physics. Combined with years of hard work he managed to build up this experiment and I am very grateful for his help inside and outside of the doors of our lab.

The amount of help Lothar Ratschbacher provided to me and others are huge. His ideas and supervision really increased the quality of this work which I really appreciate.

The tea breaks Dr. Wolfgang Alt organizes are not only a great opportunity to learn about physics electronics, engineering and philosophy but are also a reason for the very nice atmosphere in this group. I want to thank him for those tea breaks and his excellent taste regarding fruits and candies.

I want to thank the complete Meschede group for the possibility to work together with so many impressively motivated people.

Last but not least I want to thank my parents for their support.

I hereby declare that this thesis was formulated by myself and that no sources or tools other than those cited were used.

Bonn, .....  
date

.....  
signature